RESEARCH ARTICLE

PALEOANTHROPOLOGY

Contemporaneity of *Australopithecus*, *Paranthropus*, and early *Homo erectus* in South Africa

Andy I. R. Herries[1,2]*†, Jesse M. Martin[1]†, A. B. Leece[1]†, Justin W. Adams[3,2]†, Giovanni Boschian[4,2]†, Renaud Joannes-Boyau[5,2], Tara R. Edwards[1]‡, Tom Mallett[1], Jason Massey[3,6], Ashleigh Murszewski[1], Simon Neubauer[7], Robyn Pickering[8,9], David S. Strait[10,2], Brian J. Armstrong[2], Stephanie Baker[2], Matthew V. Caruana[2], Tim Denham[11], John Hellstrom[12], Jacopo Moggi-Cecchi[13], Simon Mokobane[2], Paul Penzo-Kajewski[1], Douglass S. Rovinsky[3], Gary T. Schwartz[14], Rhiannon C. Stammers[1], Coen Wilson[1], Jon Woodhead[12], Colin Menter[13]

Understanding the extinction of *Australopithecus* and origins of *Paranthropus* and *Homo* in South Africa has been hampered by the perceived complex geological context of hominin fossils, poor chronological resolution, and a lack of well-preserved early *Homo* specimens. We describe, date, and contextualize the discovery of two hominin crania from Drimolen Main Quarry in South Africa. At ~2.04 million to 1.95 million years old, DNH 152 represents the earliest definitive occurrence of *Paranthropus robustus*, and DNH 134 represents the earliest occurrence of a cranium with clear affinities to *Homo erectus*. These crania also show that *Homo*, *Paranthropus*, and *Australopithecus* were contemporaneous at ~2 million years ago. This high taxonomic diversity is also reflected in non-hominin species and provides evidence of endemic evolution and dispersal during a period of climatic variability.

Remnants of infilled and eroded cave systems (palaeocaves) formed within the Malmani dolomite in northeastern South Africa have yielded one of the richest early hominin records in the world, including *Australopithecus africanus*, *Australopithecus sediba*, *Paranthropus robustus*, and early *Homo* (Fig. 1) (*1*–*6*). Most of these hominin species are endemic to southern Africa, with only the early *Homo* material being potentially conspecific with hominins in eastern Africa (*1*–*4*), where the origins of *Homo* have been suggested to occur much earlier (*7*). However, the fragmented nature of most South African early *Homo* specimens (such as StW 53, SK 15, and SK 847) makes the taxonomy of this group and its relationship to eastern African *Homo* uncertain, with many fossil specimens assigned to multiple species or genera (*4*). An alternative hypothesis is that *A. sediba* could be the ancestor of South African *Homo* (*8*), despite being known from only ~2 million years (Ma) ago (*9*, *10*).

The majority of Early Pleistocene hominin specimens from South Africa come from the Sterkfontein, Swartkrans, and Kromdraai B palaeocaves, located within 3 km of each other in the Blaauwbank Stream Valley, ~40 km northwest of Johannesburg in Gauteng Province (Fig. 1C) (*3*–*6*). Before 1992, the only other early hominin fossils known from South Africa were the 40 specimens from the Makapansgat Limeworks (~260 km to the north) and the single specimen from the Buxton-Norlim Limeworks (Taung Child; 360 km to the southwest) (Fig. 1B) (*6*). Moreover, all the discoveries of new early hominin fossils in the past 30 years have come from an area of karst roughly 40 by 12 km (Fig. 1), referred to here as the "Gauteng Malmani" (Fig. 1C). The pattern of hominin evolution in South Africa before ~1.1 Ma ago is thus biased geographically because of the limited extent of the Malmani dolomite karst from which all the fossils derive (*5*, *6*). Correlation of the South African hominin record to that in eastern Africa has been limited by the perceived stratigraphic complexity of many of the South African sites as well as the historic difficulty in dating palaeokarst owing to a lack of suitable material for radiometric dating (*5*, *6*). Until recently, most dates for South African sites were based on biostratigraphic correlation with the better-dated eastern African sites some 3000 to 4000 km away (*5*, *6*).

The stratigraphic sequences at most South African palaeocave sites have been defined according to a lithostratigraphic approach in which breccia deposits and siltstone deposits have been classified as sequential numbered Members, thought to represent different temporal phases of deposition (*11*–*14*). In some cases, in which stratigraphic contacts can be identified, older lithofacies have clearly collapsed, subsided, or been eroded by secondary cave-formation processes before later lithofacies infilled the resulting space (*15*). This often leads to complexities such as deposits formed by reworking of older units and thus mixing of fossil material (*5*, *15*, *16*). In other cases, in which stratigraphic links are obscured, the relationship of different lithologies is less certain, and the depth that deposits have been accumulated within the cave has been used to suggest that this also represents temporal depth, even when a continuous depositional sequence cannot be identified (*6*, *13*). However, caves do not always conform to the law of superposition, and deposits can be inverted or reworked or contain intrusive events (*5*, *16*–*18*). At other sites, where mining or erosion has not obscured stratigraphic relationships, it is clear that different lithofacies represent different depositional processes happening in separate parts of the cave simultaneously, with grading between the different defined Members (*19*, *20*). The Members thus bear little relation to chronostratigraphy, and there is profound lateral variation in lithology within what should strictly be defined as a single Member. Misinterpreting these complexities has led to much confusion when defining the stratigraphy of the sites, which often requires a well-resolved chronology for robust interpretation (*5*, *6*, *15*, *19*).

With the advent of uranium-lead (U-Pb) geochronology as a method for dating Pliocene and Pleistocene speleothems, it became possible to date the flowstones that underlie and cap fossil-bearing deposits, creating datable flowstone-bound units (FBUs) (*21*, *22*). Dating of flowstones across the Gauteng Malmani revealed their contemporaneous formation in multiple caves between ~3.2 and ~1.3 Ma ago (*21*). As such, flowstones can be used to derive a regional chronology in the same way as volcanic tuffs in eastern Africa (*21*). However, capping and underlying flowstones have been removed by mining and/or surface erosion at some sites (*19*), and the dating of flowstones alone may only provide broad age ranges for the associated fossil-bearing cave sediments between them (*21*). It is therefore critical to combine U-Pb dating with other complementary

[1]Palaeoscience, Department of Archaeology and History, La Trobe University, Bundoora, 3086 VIC, Australia. [2]Palaeo-Research Institute, University of Johannesburg, Johannesburg, Gauteng Province, South Africa. [3]Department of Anatomy and Developmental Biology, Biomedicine Discovery Institute, Monash University, VIC, Australia. [4]Department of Biology, University of Pisa, Pisa, Italy. [5]Geoarchaeology and Archaeometry Research Group (GARG), Southern Cross University, Military Road, Lismore, 2480 NSW, Australia. [6]Department of Integrative Biology and Physiology, University of Minnesota Medical School, Minneapolis, MN, USA. [7]Department of Human Evolution, Max Planck Institute for Evolutionary Anthropology, 04103 Leipzig, Germany Germany. [8]Department of Geological Sciences, University of Cape Town, Cape Town, Western Cape, South Africa. [9]Human Evolution Research Institute, University of Cape Town, Cape Town, Western Cape, South Africa. [10]Department of Anthropology, Washington University in St. Louis, St. Louis, MO, USA. [11]Geoarchaeology Research Group, School of Archaeology and Anthropology, Australian National University, Canberra, ACT, Australia. [12]Department of Earth Sciences, University of Melbourne, Melbourne, VIC, Australia. [13]Department of Biology, University of Florence, Florence, Italy. [14]Institute of Human Origins, School of Human Evolution and Social Change, Arizona State University, Phoenix, AZ, USA.
***Corresponding author. Email: a.herries@latrobe.edu.au**
†These authors contributed equally to this work.
‡Present address: Department of Geological Sciences, University of Cape Town, University Avenue S, Rondebosch, Cape Town, 7700 Western Cape, South Africa.

methods, such as uranium-series electron spin resonance (US-ESR) dating and palaeomagnetism (*5*, *6*, *15*, *19*). Because complex depositional situations can occur in caves, such as speleothem false floors, it is also important to show the nature of the contact between sediments and dated speleothem by using micromorphology.

Recent geochronological work in the Gauteng Malmani suggests a transition occurs between ~2.3 and ~1.8 Ma ago from supposedly older sites containing *Australopithecus* (Malapa, Sterkfontein Member 4) to supposedly younger sites containing *Paranthropus* and *Homo*, together with the first bone and stone tools (Gondolin, Kromdraai B, Sterkfontein Member 5, and Swartkrans Member 1) (Fig. 1C) (*5*, *6*, *9*, *15*, *21*, *23*–*25*). At the same time, there was a turnover in other fauna as South African environments became more arid (*26*–*29*). However, coarse chronological resolution and imprecise provenance of historically collected fossils (*5*) enable limited interpretations of how and when faunal communities changed and whether *Paranthropus* and/or supposed early *Homo* fossils directly relate to earlier *Australopithecus* species or dispersed into the region and ultimately replaced them.

Work on sites outside the Blaauwbank Stream Valley has expanded our understanding of the South African record and revealed that not all palaeocave sites have complex multigenerational phases of karstification and infill (*9*, *19*), as documented at sites such as Sterkfontein, Swartkrans, and Kromdraai (*5*, *6*, *15*, *17*). Discovered in 1992, the Drimolen palaeocave complex (Fig. 1, C and D) is one such site (*30*). Drimolen has yielded more than 155 hominin specimens (*1*, *31*), together with substantial collections of other fauna (*32*), bone tools (*25*), and a small assemblage of Mode 1 stone tools (*24*). The younger part of the

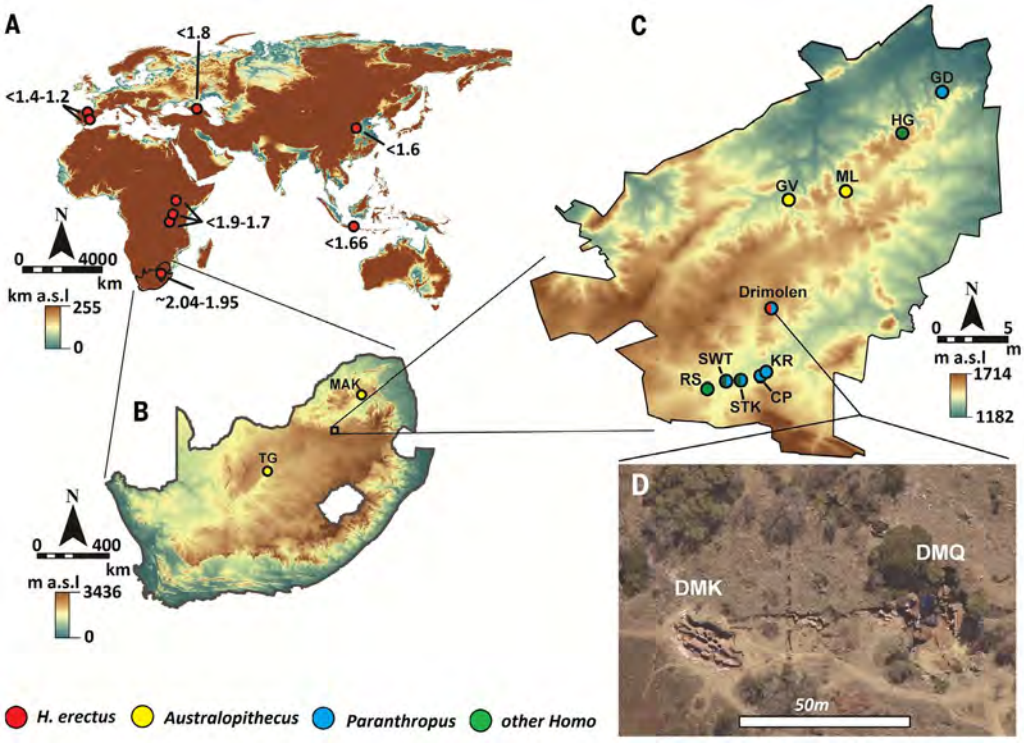

Fig. 1. The Location of the Drimolen palaeocave complex. (**A**) The location of Drimolen in comparison with other *H. erectus* sites worldwide and their approximate maximal age. (**B**) The location of Drimolen within South Africa in relation to other early hominin fossil sites and the Gauteng Malmani sites. (**C**) The location of Drimolen within the Gauteng Malmani in relation to other hominin sites. The Blaauwbank Stream Valley is represented by sites running from Bolt's Farm (BF) to Kromdraai (KR). CP, Coopers D; STK, Sterkfontein (also contains *Australopithecus*); SWT, Swartkrans; RS, Rising Star; GV, Gladysvale; ML, Malapa; HG, Haasgat; GD, Gondolin. Colors indicate the predominant genus or species represented. (**D**) An aerial view of the Drimolen site and the relationship of the hominin-bearing DMQ (2.04 to 1.95 Ma) and nonhominin-bearing DMK (~2.61 Ma).

Table 1. Palaeomagnetic data, associated US-ESR and U-Pb ages and age ranges for the various deposits at DMQ. Dec, declination; Inc, inclination; K, K parameter; Plat, palaeolatitude; WC, Warthog Cave; WOJ, Walls of Jericho; FS, flowstone; SS, sandstone and siltstone; N, normal; I, intermediate; R, reversed.

Sample	Location	Depth	Type	Dec	Inc	K	Plat	Polarity	U-Pb/ESR (Ma)	Combined date (Ma)	Fossil
DN09	WC	−3.90	FS	16.5	−63.7	141.4	66.5	N	1.79 ± 0.10	1.89 to 1.78	
DN27	WOJ	0.04	SS	11.7	−23.2	40.3	72.3	N		1.95 to 1.78	
DN24	WOJ	−0.45	SS	16.9	−21.0	149.3	68.0	N		1.95 to 1.78	
DN26	WOJ	−0.59	SS	42.7	−12.0	64.5	44.7	I		~1.95	
DNFS3	WOJ	−0.78	FS	242.1	−53.8	62.2	−5.8	I	1.96 ± 0.11	~1.95	
DN19	WOJ	−1.02	SS	222.3	28.6	174.7	−48.4	I	1.97 ± 0.15	~1.95	
DN21	WOJ	−1.55	SS	258.2	29.4	337.6	−17.0	I		~1.95	
DN29	WOJ	−1.71	SS	153.8	38.3	41.4	−65.7	R		2.28 to 1.95	
DN08	WOJ	−1.90	SS	156.9	29.6	56.0	−61.6	R		2.28 to 1.95	
DN01	WC	−3.33	SS	167.4	17.1	139.0	−69.0	R		2.28 to 1.95	DNH 152
DN03	WC	−4.36	SS	188.4	26.7	180.7	−75.8	R	2.04 ± 0.24	2.28 to 1.95	DNH 134
DN39	WC	−6.40 to -80	FS	26.5	−29.1	156.9	63.1	N	2.67 ± 0.10	2.77 to 2.61	

Drimolen system, known as Drimolen Main Quarry (DMQ), is best known for the 1994 discovery of the DNH 7 cranium, the most complete *P. robustus* skull found to date (*1*). Much of the rest of the DMQ hominin material consists of isolated teeth (*31*). However, in 2015 and 2018, two new hominin crania were discovered that represent *Homo* (DNH 134) and *Paranthropus* (DNH 152). These recent fossil finds, together with a well-resolved chronology at DMQ, now make it possible to address in greater detail the complex period of change in hominin evolution that occurred around 2 Ma ago and set a standard for dating fossil-bearing palaeokarst.

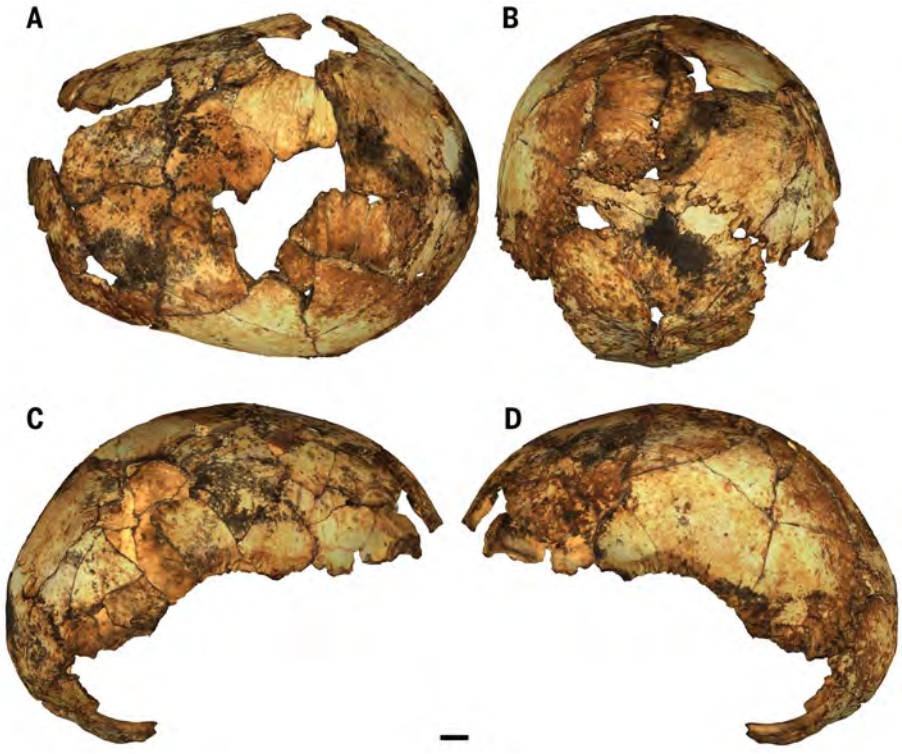

Fig. 2. The DNH 134 *Homo* aff. *erectus* neurocranium. (**A**) Superior view, anterior to the left. (**B**) Posterior view. (**C**) Right lateral view, anterior to right. (**D**) Left lateral view, anterior to the left. Scale bar, 10 mm.

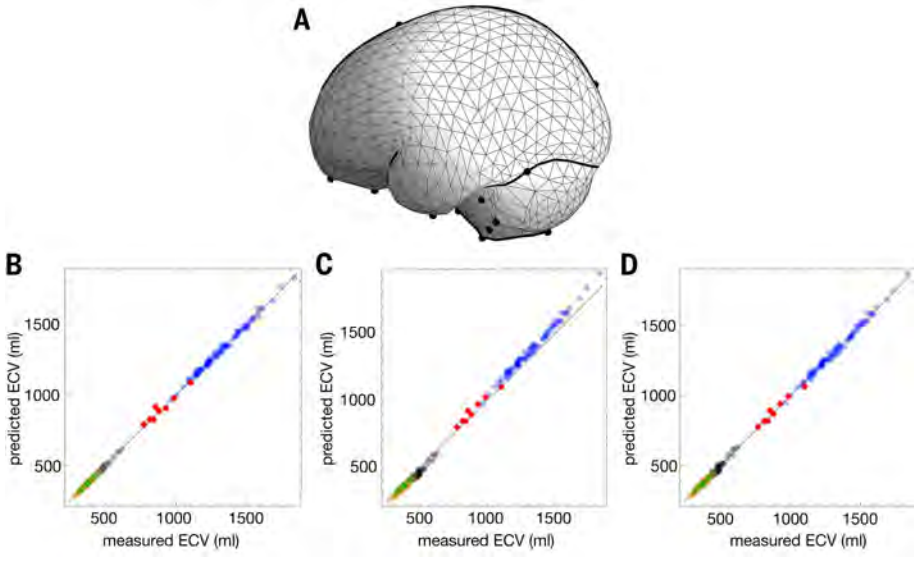

Fig. 3. Endocranial volume estimation of DNH 134. (**A**) Endocranial landmark set used for extracellular volume (ECV) estimation. Each vertex of the surface is used as a landmark or semilandmark. Anatomical landmarks are shown as spheres, and curve semilandmarks are connected as black lines. (**B** to **D**) Measured versus predicted ECV [(B) regression-based, (C) pooled treatment planning system (TPS)–based, and (D) species-specific TPS-based estimates] for human (blue), *H. erectus* (red), gorillas (gray), orangutans (orange), and chimpanzees (green).

The DNH 134 *Homo* aff. *erectus* cranium

DNH 134 comprises a partial neurocranium (Fig. 2) that preserves most of the occipital squama, parietals, and frontal squama, with no evidence of plastic deformation. The cranial sutures are patent and at an early stage of fusion, indicating that the specimen is a juvenile. The metopic suture is fused externally, and the anterior and posterior fontanelles are absent, indicating an age at death greater than 12 to 36 months according to modern human standards (*33*, *34*). The parietals exhibit two tables of bone separated by diploë, indicating that DNH 134 was ontogenetically older than the Mojokerto juvenile [(*35*–*36*), but see (*37*)]. To estimate cranial capacity, we created a partial virtual endocast and used multivariate statistics based on three-dimensional (3D) landmark data of a reference sample (Fig. 3 and Materials and methods). The endocranial volume as predicted by means of linear regression is 538 cm^3, with a 95% single prediction band from 514 to 564 cm^3. Estimates based on multiple thin-plate spline reconstructions have a larger range but are consistent with this estimate (484 to 593 cm^3). Thus, estimated brain size in the juvenile DNH 134 overlaps with the high end of the range of adult *Australopithecus* and *Paranthropus* but exceeds the brain sizes (275 to 410 cm^3) of juvenile *Australopithecus* (*2*, *38*–*39*). Although extrapolation of an adult cranial capacity is not straightforward, it is clear that at this ontogenetic stage, DNH 134 has not reached adult size but possesses a cranial capacity at the lower range of adult variation of the population from which it was drawn. Assuming an age at death between 2 and 3 years, DNH 134 could have reached a cranial capacity between 588 and 661 cm^3 or 551 and 577 cm^3 according to a human or a chimpanzee growth model, respectively.

The specimen preserves characters that align it morphologically with *H. erectus sensu lato* (including *Homo ergaster*): Its profile is "teardrop" shaped in superior view; its squamosal suture is nearly straight; sagittal keeling is present on the frontal and parietals; the cranial vault is long and low, with strong sagittal occipital curvature and lambdoidal flattening; and although the anterior aspect of the foramen magnum is missing, it is evident that a basion-bregma chord would have been short. These traits together distinguish DNH 134 from *A. africanus*, *P. robustus* (as preserved in DNH 7), *Homo habilis*, *Homo rudolfensis*, and *Homo naledi* (*40*). Individually, none of these traits is fully diagnostic of *H. erectus s.l.*, which is morphologically variable across time and space (*41*),

yet collectively, they strongly suggest an affinity with that species. DNH 134 is strikingly similar to the Mojokerto *H. erectus* cranium in overall cranial shape (Fig. 4).

The DNH 152 *P. robustus* cranium

DNH 152 is a partial cranium that preserves much of the left side of the parietal and frontal bones, a portion of the occipital, the right temporal, the lateral margin of the right orbit, as well as four teeth: left and right maxillary first and maxillary second molars (Fig. 5). The right dental elements are in situ within a portion of the maxilla, whereas the left elements are isolated. The specimen preserves a number of characters that align it taxonomically with *P. robustus*. The supraglenoid gutter is partially preserved and would have been wide. The mastoid process is inflated lateral to the supramastoid crest, from which it is separated by a broad shallow groove. The external auditory meatus is large and nearly circular (11.8 by 11.5 mm), positioned lateral to the tip of the mastoid process and nearly at the level of the suprameatal crest. The post-glenoid process is small and fused to the tympanic. Although the tips of the articular tubercle and entoglenoid process are missing, it is evident that the articular eminence was wide and that the glenoid fossa was deep. The digastric groove takes the form of a narrow notch. The superior temporal line on the frontal bone is a well-demarcated ridge, suggesting that a frontal trigon would have been present, but this cannot be directly observed. The sagittal crest bifurcates superior to lambda, leaving a bare area on the occipital, and the temporal lines meet the nuchal line in the lateral third of its extent, forming a short, partial compound temporonuchal crest. There are extensive striations and beveling on the inferior aspect of the left parietal bone, indicating that the overlap between the temporal and parietal bones at the squamosal suture was extensive. The inferior orbital margin is rounded laterally. Both molars evince a quadrangular occlusal outline with mesiobuccal extension, a deep and narrow central fossa and longitudinal fissure, and a thick distal marginal ridge typical of *P. robustus*. The left M^1 is fractured and shows "hyper-thick" enamel. On the basis of these characteristics, the cranium has been assigned to *P. robustus*.

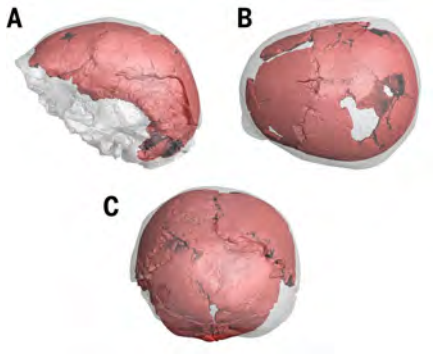

Fig. 4. Comparisons of the DNH 134 cranium with the Mojokerto juvenile *H. erectus* cranium. DNH 134 (red) superimposed on the Mojokerto cranium (gray) after scaling both specimens to the same bregma–inion length. (**A**) Left lateral view, anterior to left. (**B**) Superior view, anterior to left. (**C**) Posterior view.

Morphology of the DMQ palaeocavern

The Drimolen palaeocave system consists of at least two temporally and spatially distinct cave infills: the ~2.61-Ma-old Drimolen Makondo (DMK) deposit (*19*) and the hominin-bearing DMQ (Fig. 1C) (*27*–*29*). DMQ is a large palaeocavern (~20 by 15 m) formed in one of the highest current exposures of the Gauteng Malmani (~1545 m above mean sea level). On the basis of current topography, the palaeocavern had a very small watershed and acted as a vertical pothole sink for groundwater. The nearby Wonder Cave (also known as van Wyk's Main Cave) (*42*) provides a good modern analogy. By contrast, cave sites in the Blaauwbank Stream Valley, such as Sterkfontein and Plovers Lake, act as valley bottom "collecteur" caves, estavelles or exsurgences where underground lakes occur either intermittently or permanently (*43*). Although the landscape in the Gauteng Malmani has been altered over the past few million years because of erosion (*9*), this would not have substantially changed the watershed of the Drimolen palaeocave owing to its location near the top of a hill, rather than within an actively incised valley. Moreover, only ~10 m of erosion is estimated per million years on the hill behind DMQ (*43*). If washed in, the sediments, fossils, and archeology deposited in DMQ would have originated from a restricted landscape around the cave.

Today, DMQ is a roughly subcylindrical karstic depression with vertical sides, about 5 to 8 m deep. Most of the ceiling and the upper parts of the DMQ cavern infill have been lost to erosion, breakdown, and dissolution (Figs. 1 and 6). The outline of the current quarry

Table 2. US-ESR dating data for DMQ-2 and DMQ-3 fragments.

Sample	DMQ-2	DMQ-3
Enamel		
Dose (Gy)*	1814 ± 59	2414 ± 76
U [parts per million (ppm)]†	1.43 ± 0.15	2.07 ± 0.18
234U/238U†	1.2841 ± 0.0587	1.0886 ± 0.0369
230Th/234U†	0.9220 ± 0.0256	0.9731 ± 0.0155
Thickness (m)	1354 ± 189	1551 ± 320
Water (%)	3 ± 1	3 ± 1
Dentine		
U (ppm)†	17.30 ± 1.11	19.31 ± 1.05
234U/238U†	1.4110 ± 0.0237	1.4183 ± 0.0109
230Th/234U†	0.9558 ± 0.0201	0.8822 ± 0.0278
Water (%)	5 ± 3	5 ± 3
Sediment		
U (ppm)	1.9 ± 0.5	1.9 ± 0.5
Th (ppm)	3.02 ± 0.2	3.02 ± 0.2
K (%)	0.29 ± 0.05	0.29 ± 0.05
Water (%)	15 ± 10	15 ± 10
External dose rate sediment		
Beta dose (μGy a^{-1})	44 ± 9	38 ± 8
Gamma dose (μGy a^{-1})	323 ± 39	323 ± 39
Cosmic (μGy a^{-1})	97 ± 50	97 ± 50
Combine US-ESR age		
Internal dose rate (μGy a^{-1})‡	291 ± 80	701 ± 76
Beta dose dentine (μGy a^{-1})‡	134 ± 37	69 ± 8
P enamel‡	0.64 ± 0.13	−0.45 ± 0.01
P dentine‡	0.03 ± 0.02	1.46 ± 0.15
Total dose rate (μGy a^{-1})‡	889 ± 109	1228 ± 100
Age (thousand years)‡	2041 ± 240	1965 ± 147

*Dose-equivalent (DE) obtained using McDoseE 2.0, with SSE [from (*101*)]. †Uranium concentration values were obtained by means of LA-MC-ICPMS and LA-ICPMS on both teeth and both dental tissues. ‡The age was calculated by use of (*50*), with the dose rate conversion factors of (*110*), and the enamel and dentine density of 2.95 and 2.85, respectively, from (*111*).

was created through speleothem (lime) mining in the late 19th century. The pattern of mining indicates that speleothem deposition originated on the eastern side of the palaeocavern. Water forming these speleothems flowed downslope along the bedding of the Malmani dolomite (to the northwest) to form a thinning flowstone floor on the southwestern side of the cavern. The combination of natural erosion and dissolution and anthropogenic mining has produced a range of stratigraphic profiles that exposes the entire formational history of the cavern (Figs. 6 to 10).

The western part of DMQ consists of a 10-m-wide belt of in situ calcified palaeocave sediments adhering to the western dolomite wall of the DMQ palaeocavern and deposited over a remnant of basal flowstone (BFS). These in situ deposits consist of calcified sediment pinnacles up to 3 m high, shaped through subcutaneous secondary karstic dissolution. The spaces between these pinnacles (makondos) (*19*) are filled with soft sediment that represents the in situ decalcified equivalent of the sediment in the pinnacles, and articulated bone can be found embedded across the contact of both mediums (*19*). Both DNH 134 and DNH 152 were recovered partly from decalcified and partly from lightly calcified breccia and in close contact to solid breccia. Directly to the east of these in situ deposits is a mixture of collapsed and decalcifying palaeocave deposits and miner's rubble that was the focus of excavations between 1992 and 2016 (*30*). This "Central Excavation Area" has yielded most of the fossil material but is mostly ex situ. This includes the DNH 7 *P. robustus* cranium (*1*) that comes from a large block (Eurydice Block) (Fig. 6) in the center. Fossil material in this collapse zone and in the center of makondo features (*19*) often shows poorer preservation, which is why the majority of hominin fossils recovered to date consist of isolated teeth (*31*). The collapse of this breccia was caused by the undermining of the in situ deposits during lime-mining, forming the Inner Cave (Fig. 7). Although secondary cave formation has also occurred at DMQ, it is limited to the formation of Warthog Cave at the contact between the palaeocavern infill and the southern dolomite wall of the palaeocavern (Fig. 7). Warthog Cave has only slightly eroded into the palaeocave fill, and the only fossil to have been recovered from the fill is an isolated *Paranthropus* molar (DNH 122) that lay very close to the contact with the palaeocave deposits. There is no evidence that this cave has affected

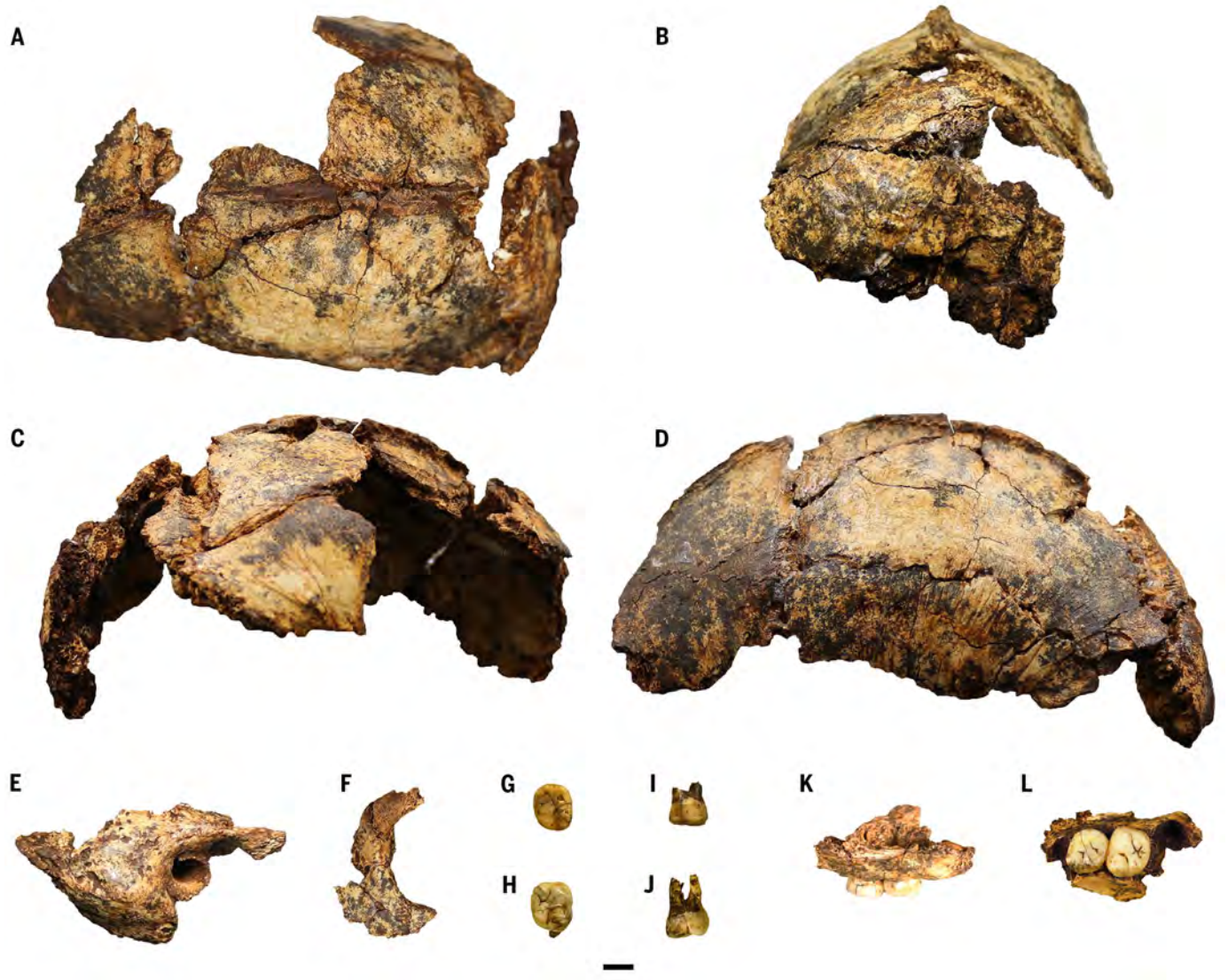

Fig. 5. The DNH 152 *Paranthropus robustus* cranium. (**A**) Superior. (**B**) Posterior. (**C**) Right lateral. (**D**) Left lateral. (**E**) Right temporal. (**F**) Right orbit. (**G**) Left M1 occlusal. (**H**) Left M2 occlusal. (**I**) Left M1 buccal. (**J**) Left M2 buccal. (**K**) Right M1 and M2 buccal. (**L**) Right M1 and M2 occlusal. Scale bar, 10 mm.

the palaeocave deposits through other mechanisms, such as collapse.

Stratigraphy of the DMQ palaeocavern

We outline the geochronology and stratigraphy of the DMQ palaeocavern as recorded in a number of key stratigraphic sections along the mined and excavated exposures of the in situ western wall palaeocave deposits (movie S1). The various lithofacies described in table S1 have been identified by means of stratigraphic analysis and micromorphology (*44*). The deposits represent a process of continuous accumulation, erosion, and reworking of a single, large clast-supported talus cone breccia (CSB) that formed on a BFS beneath a vertical entrance. This talus cone was then subject to lateral winnowing during flooding to sequentially create matrix-supported breccia (MSB) and distal gravel, sandstone, and siltstone (GSS) (Figs. 11 and 12 and table S1). Micromorphological observations (Fig. 11, A and B, and table S1) indicate that the in-washing of sediment derived from the erosion of colluvial soils previously developed outside the cave. A lengthy evolution for these soils is indicated by the intense weathering of minerals and rocks (Fig. 11B). The granular microstructure of the breccia sediment mass is generally rather loose (Fig. 11A), mostly in the upper part of the breccia cone, suggesting fast deposition and winnowing of the fine particles followed by rapid cementation of the sediments. Calcite is the most common cement for both breccias and sandstone and siltstones (Fig. 11D), with the most frequent crystalline pattern being mosaic calcite, with anhedral crystals of variable size that cement the whole mass. Fragments and splinters of compact or cancellous bone, as well as microfauna, are present throughout the breccia (Fig. 11C). The breccia also contains well-preserved fragments of vegetal tissue, which exhibit cellular patterns typical of large-size monocotyledon taxa, which were likely washed in (Fig. 11C). The shape of voids in the breccia are consistent with formation by roots and/or burrowers (fig. S11C). These occur in samples from ~30 cm above the BFS, indicting the early opening of a reasonably wide entrance and thus indicating that no upper cavern existed as previously suggested (*30*).

Warthog Cave section

Warthog Cave section is the most southerly and deepest exposure of the DMQ palaeocavern fill (Fig. 7). The base of the 3-m-deep section consists of a 50-cm-thick flowstone speleothem (which was thicker before mining) that contains no notable detrital material and formed before the cavern had an opening to the surface. This BFS (−6.40 m below datum) has been U-Pb dated to 2.673 ± 0.103 Ma old (DN39A) (*21*). The normal polarity of the flowstone limits its formation to older than the Gauss-Matuyama Boundary at 2.61 Ma old (*45*), setting a lower age limit on the DMQ deposits. There is a sharp contact with an overlying fossil-bearing CSB that formed the extreme southern toe of the talus cone down the westerly dipping flowstone and represents the oldest fossil-bearing deposits at the site (Lower Cave Breccia). This unit is not noted elsewhere, has not been excavated, and is overlain by a series of well-stratified GSS deposits [Warthog GSS (WGSS)] (table S1). WGSS represents winnowing of fine-grained material from near-entrance talus deposits to the southern edge of the cavern during floods. WGSS was sampled for palaeomagnetic analysis and recorded a reversed polarity (Fig. 13 and Table 1) that is consistent with being deposited between BFS and WCFS, between 2.61 and 1.95 Ma ago. WGSS filled the southern part of the palaeocavern to the low stepped roof that now forms the top of Warthog Cave. The top of WGSS has been eroded and capped by a 15-cm-thick flowstone [Warthog Cave Flowstone (WCFS)] (−3.90 below datum), which infilled an erosional channel between the palaeocave deposits and the western dolomite wall of the palaeocavern. The flowstone dates to 1.789 ± 0.104 Ma ago by means of U-Pb dating (DN09) (*21*) and recorded a normal magnetic polarity (Fig. 13 and Table 1) that is consistent with deposition during the Olduvai SubChron (1.95 to 1.78 Ma ago) and indicates its formation 170,000 to 60,000 years after the deposition of the WGSS deposits on which it lies (*45*).

Jangi buttress

The Jangi buttress occurs just to the north of the Warthog Cave section at the southwest edge of the Central Excavation Area, in the center of the site (Fig. 8). The Jangi buttress comprises a 3-m-deep outcrop of CSB (table S1), representing a talus cone breccia formed from a vertical entrance and accumulated against the western wall of the palaeocavern overlain by MSB (table S1). The breccia consists of large angular-to-subangular dolomite and chert blocks (up to ~40 cm) formed through entrance and roof collapse, with small pockets of fine-grained in-washed sediment, often with dense macrofossils, occurring between the blocks. A continuous outcrop of CSB extends from the Jangi buttress west to the Western Wall and then north to the Italian Job pinnacle (Fig. 6). Adhering to the Jangi buttress on its northern side (western wall of Central Excavation Area) are decalcified remnants of CSB. Excavation of this decalcified material mimics the nature of the breccia, with pockets of yellowish red micromammal-rich sediment and ghost rock nodules consisting of the insoluble fraction of decalcified dolomite boulders and cobbles. The DNH 134 *Homo* cranium was recovered as a series of individual pieces at ~−5.31 m below datum (1.1 m above BFS) toward the base of

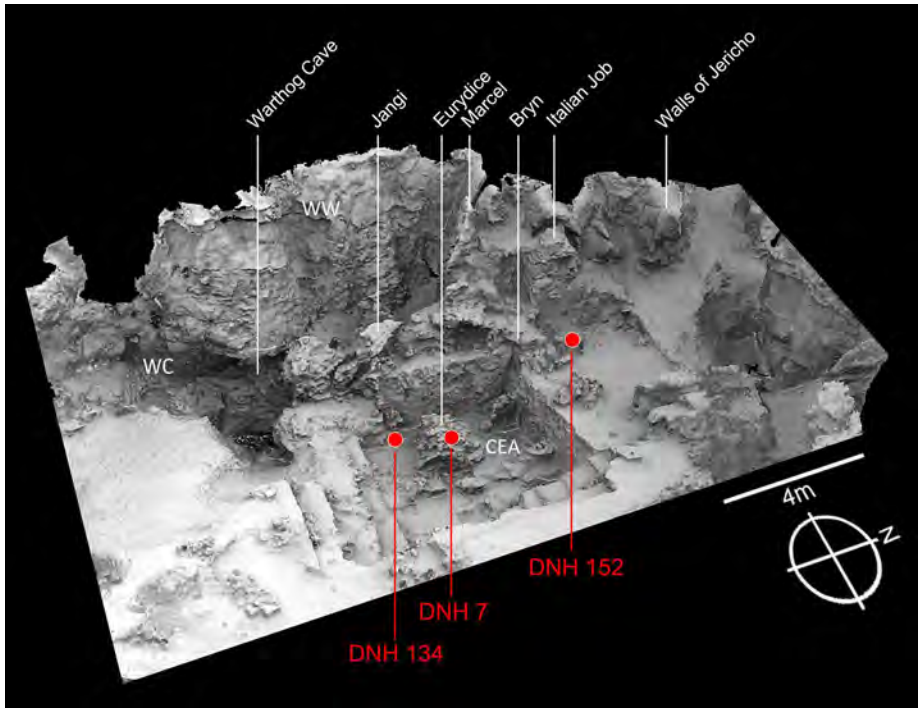

Fig. 6. 3D laser scan of DMQ. The locations of the hominin fossils DNH 7, DNH 134, and DNH 152 are shown relative to the main stratigraphic sections (Warthog Cave, Italian Job, Jangi, and Walls of Jericho) and features described. WC, Warthog Cave; CEA, Central Excavation Area; and WW, dolomite western wall of the palaeocavern.

the pinnacle (Fig. 8) during excavations in 2008, 2015, 2016, and 2019 (the single piece from 2008 was not recognized as hominin until more of the cranium was recovered in 2015). The cranial pieces were partly recovered from lightly decalcified CSB and from decalcified sediment and collapse (since 2008 excavations) next to the pinnacle. These deposits also yielded adult *Paranthropus* teeth and bone tools. MSB and CSB of the Jangi pinnacle are equivalent to the GSS deposits of the Warthog Cave section and represent the talus cone from which the WGSS deposits were winnowed. A US-ESR age from a bovid tooth next to the cranium gave an age of 2.041 ± 0.240 Ma (Fig. 8), further confirming this association, and shows that the WGSS and Jangi buttress CSB sediments were deposited ~600,000 to 280,000 years after BFS formed at >2.61 Ma ago.

The Italian Job pinnacle section

The Italian Job pinnacle section is located just to the northwest of the Central Excavation Area (Fig. 9) and occurs stratigraphically higher than the Jangi pinnacle, with which it is connected by in situ breccia that also connects both sections to the west wall of the palaeocavern. The Italian Job pinnacle consists of an intermediate facies of MSB (table S1) that represents a vertical and lateral transition from CSB at the core of the central talus cone to MSB at the cone's edge. This transition occurs as fine sediment begins to dominate over large clast deposition during the vertical and westward expansion of the central debris cone. It also represents a lateral transition from MSB of the upper part of the central debris pile to GSS deposits that occur on the northern side of the Italian Job pinnacle itself and in the Walls of Jericho pinnacle on the northern edge of the palaeocavern. This transition represents winnowing of fine-grained sediment from the central talus cone to the northern corner of the cavern during floods. A thin flowstone [Walls of Jericho Flowstone (WOJFS)] occurs at −0.97 m below datum in the Italian Job pinnacle and continues into and through the adjacent Walls of Jericho pinnacle, suggesting a slight hiatus in deposition. US-ESR dating of a bovid tooth from ~18 cm below the flowstone at −1.15 m below datum produced an age of 1.965 ± 0.147 Ma. The DNH 152 *P. robustus* cranium was recovered from the very base of the current excavated exposures of the Italian Job at a height of −3.15 m below datum and ~2.18 m below the WOJFS.

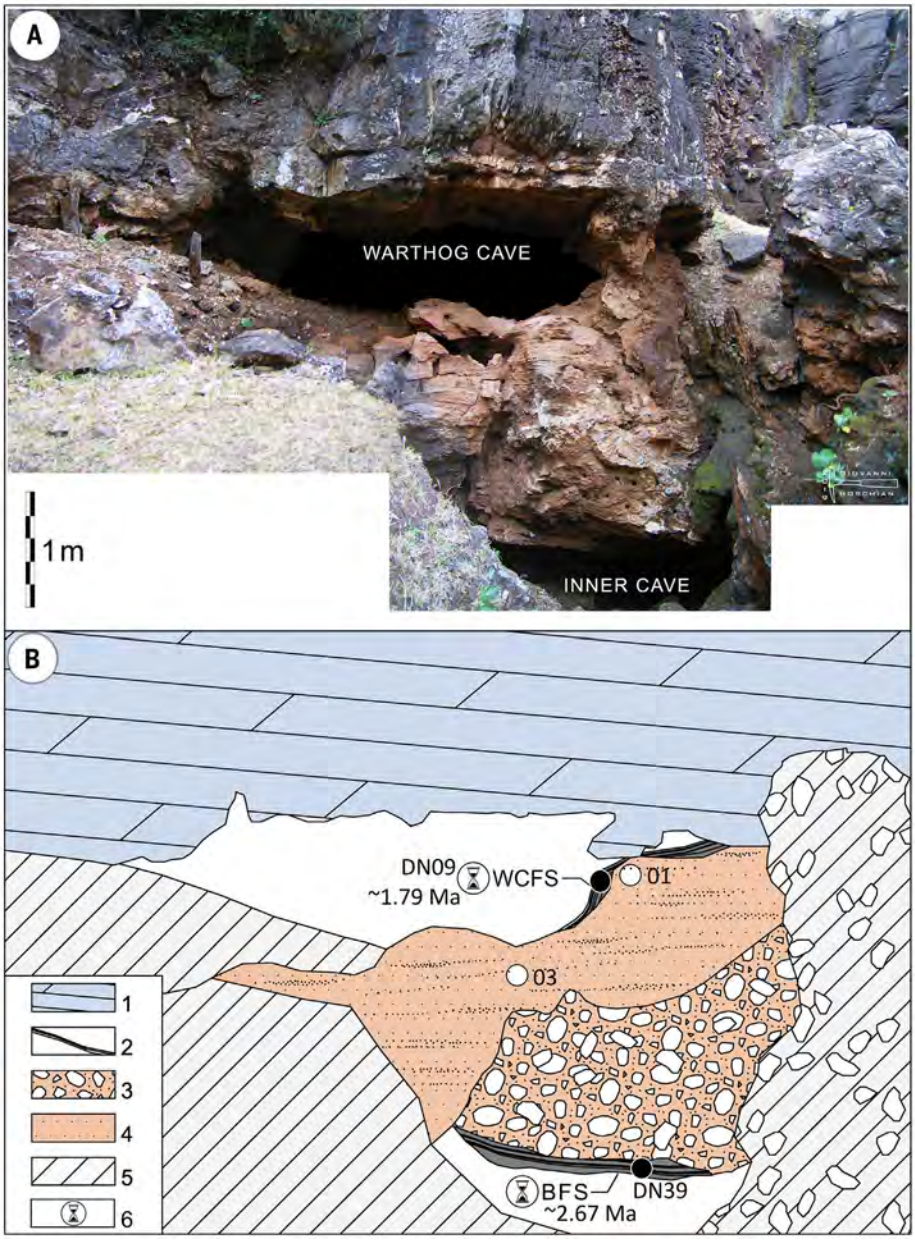

Fig. 7. Warthog Cave section showing palaeomagnetic and U-Pb and sample locations. (**A**) Photograph and (**B**) section showing stratigraphy and geochronometric data. 1, dolomite bedrock; 2, flowstone (BFS); 3, clast-supported breccia (CSB); 4, sandstone/siltstone (WGSS); 5, recent decalcified sediment, mine dumps and displaced blocks; 6, U-Pb sample locations: BFS (DN39A; 2.673 ± 0.103 Ma old) and WCFS (DN09 1.789 ± 0.104 Ma old). Palaeomagnetic samples are indicated by black (normal polarity) and white (reversed polarity) circles.

The Walls of Jericho pinnacle section

The Walls of Jericho pinnacle section is the most northerly exposure of the DMQ palaeocavern infill (Fig. 10). Most of the section comprises GSS, representing fine-grained sediments winnowed through medium-energy flow (Fig. 11, E and F) from the central debris pile to the south. On the northern side of the pinnacle, a steeply dipping flowstone is considered to be equivalent to the BFS in the Warthog Cave section (2.78 to 2.61 Ma) (DN39A) (*21*). As in the Warthog Cave section, there is a sharp contact between this BFS and the overlying sediments. At −0.78 m below datum, the WOJFS occurs (~2 cm thick) that has been U-Pb dated to 1.962 ± 0.107 Ma old (DN26) (*21*), which is consistent with the US-ESR age just below this flowstone in the Italian Job pinnacle. Micromorphological analysis (Fig. 12) confirms that this flowstone is not intrusive and formed during a hiatus in the deposition of GSS. GSS deposits below the WOJFS are well-laminated, whereas those above are more coarsely layered, with thin intercalated flowstones and silt crusts suggesting alternating hiatuses in clastic deposition and pooling of water (Fig. 11, G to I). Palaeomagnetic analysis indicates a change from reversed to normal polarity up through the section, with intermediate polarity occurring in the WOJFS as well as sediments above and below it, further confirming that it formed

during the deposition of the sediment sequence. On the basis of the U-Pb and US-ESR ages, this can be correlated to the reversal at the base of the Olduvai SubChron at ~1.95 Ma ago (*46*).

Geochronology

We undertook US-ESR analysis on an indeterminate medium-sized alcelaphin right maxillary third molar (right M3; DMQ-2) recovered from the lightly decalcified breccia of the Jangi buttress in direct association with the DNH 134 cranium (Fig. 8) and on another partial bovid tooth (DMQ-3) that was encased in breccia from the southern side of the Italian Job pinnacle, 2 m above DNH 152 and ~20 cm below the WOJFS (Fig. 9). We estimated the dose equivalents for DMQ-2 and DMQ-3 using the peak-to-peak T_1-B_2 method at 1814 ± 57 and 2414 ± 76, respectively (2σ error) (table S2), including an unstable radical component [neglect of core orbitals (NOCOR)] of 21 and 16%, respectively (*47*–*49*). When integrated into the US-ESR dating modeling described by Shao *et al.* (*50*), the ages of DMQ-2 and DMQ-3 are estimated to be 2.041 ± 0.240 Ma and 1.965 ± 0.147 Ma, respectively (1σ error) (Tables 1 and 2 and table S2). Both samples did not show any ratios above secular equilibrium, although the dental tissues were not extensively mapped. Nonetheless, the U-diffusion in DMQ-2 and DMQ-3 fits the open-system model, and the teeth did not exhibit obvious complex compound uranium diffusion episodes. However, the isotopic ratios between the enamel and dentine remain different, most likely indicating a more recent incorporation (uptake) of uranium in the dentine. With a U-uptake history model close to linear in most dental tissues (Table 2), as well as a rather homogenous ratio over the analyzed area, we were able to assume equilibrium in the uranium decay chain after ^{230}Th (for example, ^{210}Pb/^{230}Th = 1).

We performed palaeomagnetic analysis on the GSS and U-Pb–dated flowstones from the Warthog Cave and Walls of Jericho sections (Figs. 7 and 10 and Table 1). Natural remanent magnetization (NRM) intensities ranged from 8.94 to 0.57 Am^2/kg^1 with a mean low-frequency magnetic susceptibility (nonspeleothem samples) of 186 × 10^{-5} indicating sufficient ferromagnetic material for palaeomagnetic analysis. Mineral magnetic measurements (Fig. 13, G to I) show that both low coercivity magnetite and maghemite occur in superparamagnetic (SP), stable single domain (SSD), and vortex state (formally referred to as pseudo-single domain) (*51*) grain size ranges. Pigmentary hematite is also likely present, as indicated by a low-contribution antiferromagnetic component observed in backfield unmixing curves (Fig. 13G). This does not contribute to the NRM. A significant proportion of SP to viscous single domain (vSD) boundary grains are shown through high-frequency dependence of magnetic susceptibility (χFD%; mean 11.75% for nonspeleothem samples), and these are susceptible to more recent viscous remagnetization. First-order reversal curves (FORCs) show a predominance of single-domain signals, which are ideal for palaeomagnetism and are highlighted by closed concentric contours along the central ridge of the FORC diagram (Fig. 13H) (*52*). Given that some of the central ridge coercivity distribution intersects with the Bu axis, the SSD magnetizations are likely mixed with those of lower-coercivity SP-vSD boundary grains (*53*) in line with χFD% results. Such samples require caution when undertaking alternating field demagnetization (AF_D) cleaning to ensure that remanences associated with SSD particles were properly isolated from SP/vSD boundary overprints before their removal. FORCs also derived some influence from larger vortex state particles, as shown by a spread of remanence away from the central ridge and weak lobe features, although there is no evidence for multidomain (MD) grains, which would be reflected by a greater remanence spread along the Bu axis (*51*).

Final palaeomagnetic data for the 12 block samples are presented in Table 1 and Fig. 13. We removed viscous overprints associated with

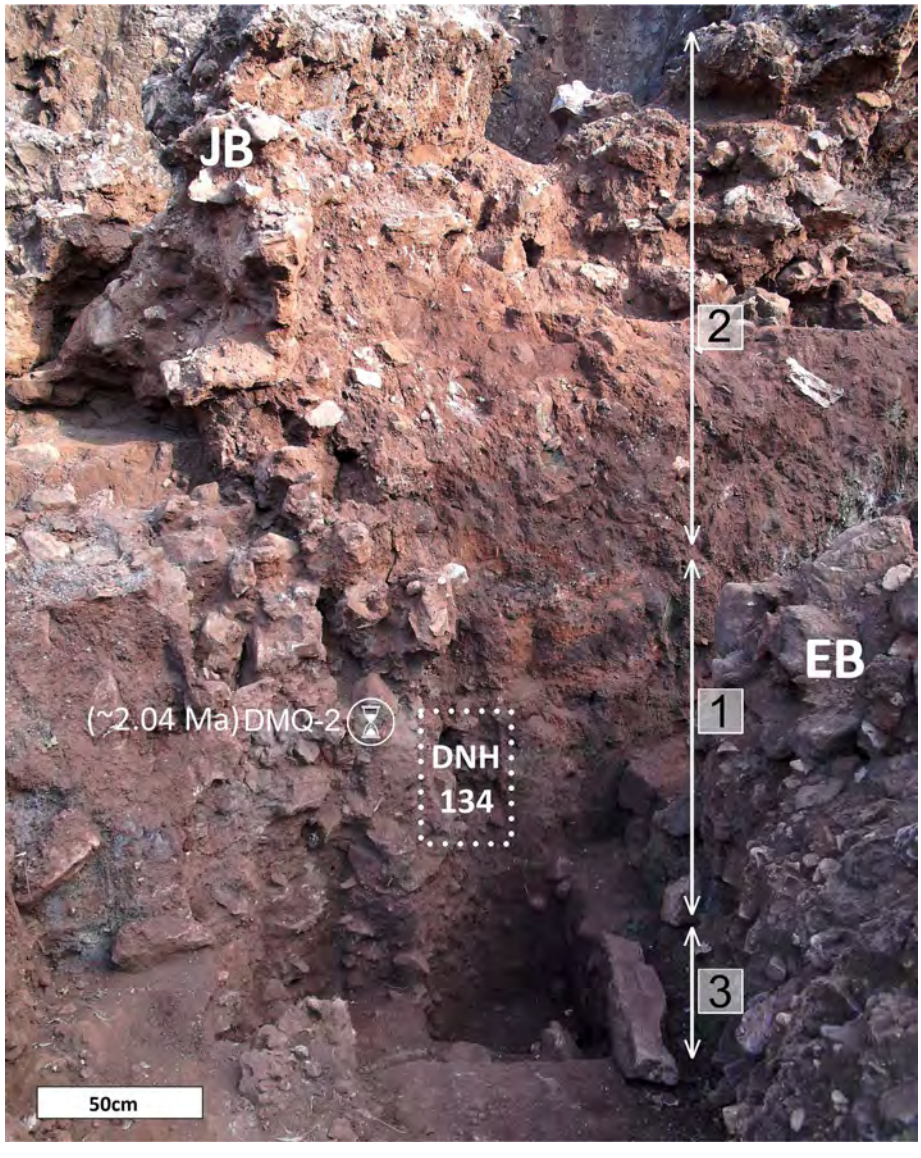

Fig. 8. Jangi Buttress section depicting DNH 134 find locus. JB, Jangi Buttress; EB, Eurydice Block. 1, CSB, with skeleton-supported structure, large chert, and decalcified dolomite (gray dusty patches) blocks and preserved, microfauna-rich reddish layers. 2, MSB with unsorted chert and subordinate dolomite clasts (the lower half is decalcified). 3, Mining rubble filling void cut underneath Jangi Buttress. The dotted rectangle depicts DNH 134 *Homo* cranium dispersion area; DMQ-2 denotes the US-ESR date 2.041 ± 0.240 Ma ago (50 cm scale).

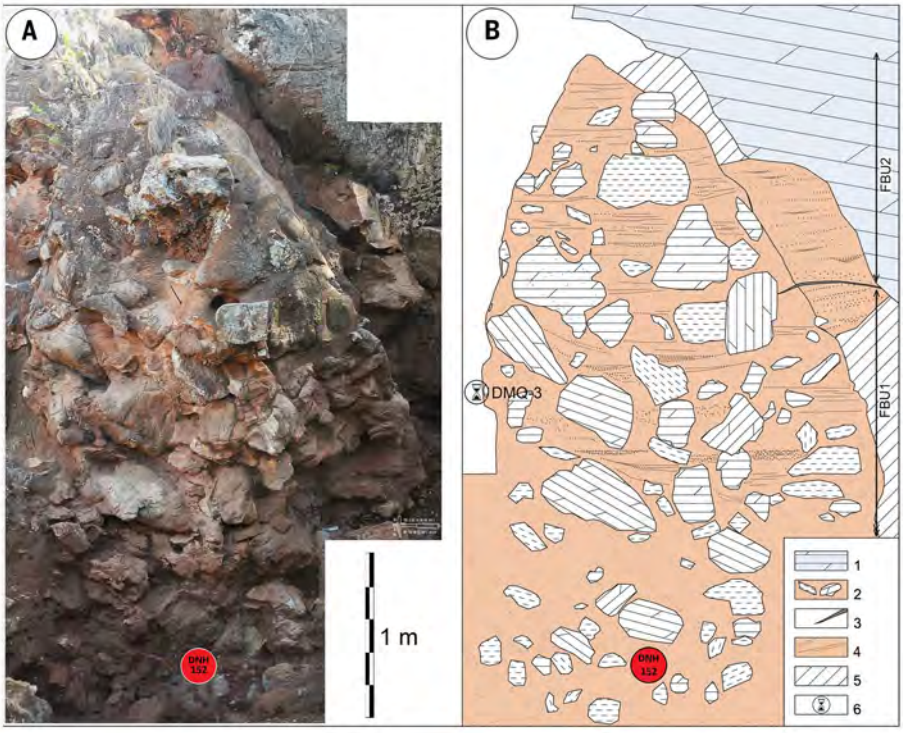

Fig. 9. Italian Job pinnacle. (**A**) Photograph and (**B**) section showing stratigraphy and geochronometric data. 1, dolomite bedrock; 2, MSB; 3, flowstone (WOJFS); 4, GSS; 5, decalcified sediment; 6, DMQ-3 denotes the US-ESR date 1.962 ± 0.107 Ma ago. The red circle indicates the DNH 152 *Paranthropus* skull location.

SP-vSD boundary grains by means of AF_D typically between 12 and 15 mT or with thermal demagnetization (TH_D) at temperatures of 250° to 325°C to reveal a single stable component of magnetization with low median angles of deflection (MADs) (<10) (Fig. 13, A to F). This characteristic remanent magnetization (ChRM) signal was removed by means of TH_D between 540 and 580°C (and 5 to 40 mT through AF_D), suggesting detrital magnetite [Curie temperature (T_c) = ~585°C] as the main remanence carrier, corroborating T_c estimates of 561° to 586°C derived from thermomagnetic (M/T) heating curves (Fig. 13I). In isolated samples, the ChRM was not removed until ~610°C, suggesting some minor maghemite contribution. Taken together, the overall stability of magnetization to high temperature along with the occurrence of reversed polarities and directional consistency among different demagnetization strategies indicates a primary remanence formed within SSD (to vortex state) magnetite and maghemite around the time of sediment deposition in the cave [depositional remanent magnetisation (DRM) or post-DRM (pDRM]. The occurrence of microlayers of flowstone within the sediments likely aided the quick lock-in of magnetic remanence and reduced any effects of pDRM. Final directions (Figs. 7, 10, 13, and 14 and Table 1) indicate a series of polarity changes throughout the sequence. Normal polarity was observed in the basal and capping flowstones of the Warthog Cave section and the upper 60 cm of the GSS of the Walls of Jericho section. Reversed polarity is noted in the GSS of the Warthog Cave section and the base of the Walls of Jericho pinnacle. The middle part of the GSS facies (−1.55 to −0.59 m below datum) in the Walls of Jericho section, as well as the WOJFS itself, record intermediate magnetic polarity that represents true intermediate geomagnetic behavior occurring during a magnetic reversal. It is extremely rare to find evidence for such reversals in terrestrial sedimentary sequences and indicates that this part of the sequence likely formed over a few to several thousand years during the reversal itself.

Chronostratigraphy and FBUs

Despite the perceived stratigraphic complexity of Gauteng Malmani palaeocaves, DMQ has a simple depositional history. Evidence suggests that the site was a water sink (pothole) that infilled over a short time frame, and there is little evidence for secondary cave formation, natural reworking of fossils, or infills of substantially different ages. Putting all the geochronological data and stratigraphic information together, the DMQ sequence can be divided into two major FBUs (Fig. 14 and Table 1). The thicker (~5.6 m thick) stratigraphically lower FBU (FBU1) occurs between the 2.673 ± 0.103–Ma-old (*16*) BFS (−6.40 m below datum) that underlies the entire sequence of clastic deposits within the palaeocavern and the 1.962 ± 0.107–Ma-old WOJFS (−0.78 m below datum) that divides the Walls of Jericho and Italian Job pinnacles (Fig. 12) (*21*). The thinner (~1.07 m), upper FBU (FBU2) formed between the WOJFS and the 1.789 ± 0.104–Ma-old WCSF (Table 1) (*21*). The normal polarity of the BFS indicates that it formed before the Gauss-Matuyama boundary at ~2.61 Ma ago (*45*), whereas the sharp contact with overlying sediments and lack of detrital inclusions confirms that the flowstone formed before an opening to the surface (as seen in base of the Warthog Cave section).

During the formation of FBU1, a large CSB was deposited beneath a vertical entrance in the western to central part of the palaeocavern (as seen in the Jangi buttress), and flooding winnowed fine-grained sediments (GSS) against the southern wall of the palaeocavern (as seen in Warthog Cave section). Between the clasts within CSB, fine-grained sediments (equivalent to GSS) and macrofossils occur in small pockets. In this early phase, articulated skeletons are often found across more than a single pocket. This indicates deposition of the skeletons before or during the deposition of blocks rather than a mechanism in which fossils and fine sediment have filtered down through a preexisting structure of blocks. The reversed polarity of the Warthog Cave GSS and US-ESR age of 2.041 ± 0.240 Ma for the oldest excavated CSB deposits from the Jangi buttress indicate that the oldest sediments, including *Homo* aff. *erectus* fossil DNH 134, entered the DMQ palaeocavern several hundred thousand years after the BFS formed and sometime between ~2.04 and 1.95 Ma ago, during the Matuyama reversed-polarity Chron. Isolated teeth of *P. robustus* and bone tools have also been recovered from these layers. As the central talus cone continued to be deposited in the central part of the cavern, it also expanded against the western dolomite wall of the cave. As the CSB of the central talus cone built up, it also graded laterally to a more MSB in the western half of the cavern (as seen in the base of the Italian Job pinnacle). At this time, when DNH 152 was deposited, the GSS deposits had already filled the cavern to the roof in its lower southern part, and GSS deposits were being winnowed against the northern wall, where the cavern roof was higher (as seen on northern edge of Italian Job and in the Walls of Jericho pinnacle). Like the top of the Warthog Cave section, the oldest deposits in the Walls of Jericho pinnacle record a reversed polarity. The DNH 152 *P. robustus* cranium was deposited during the middle part of FBU2 ~3.2 m above the BFS, 2.2 m above DNH 134, 2.2 m below the WOJFS, and ~1.6 m below the beginning of the magnetic reversal in the Walls of Jericho (Fig. 14) (*45*, *46*).

The talus cone continued to form, and as sediment was further winnowed into the northern edge of the cave (Italian Job to the Walls of Jericho section), the polarity of the GSS deposits changed from reversed to intermediate polarity, indicating the onset of a magnetic reversal. The US-ESR age of 1.965 ± 0.147 Ma for these deposits suggests that this reversal was the onset of the Olduvai Subchron at ~1.95 Ma ago. This is confirmed by the 1.962 ± 0.107 Ma U-Pb age and intermediate polarity for the thin WOJFS (DN26) (*16*) that formed during a hiatus (shorter than the few to several thousand years of a magnetic reversal) in deposition and caps the lower well-laminated GSS deposits in the northern part of the cavern (as shown in the Walls of Jericho) (Figs. 10 and 14). GSS continued to form after the WOJFS and again recorded intermediate polarity before transitioning to the normal polarity of the Olduvai Subchron just before GSS, filling up to the roof of this part of the cavern (1.95 to 1.78 Ma ago) (*46*). This indicates that the upper parts of the lower FBU, the WOJFS, and the lower part of the upper FBU were all deposited during the time frame of the magnetic reversal at the base of the Olduvai Subchron at ~1.95 Ma ago. Reversals have been estimated to take between 4000 and 22,000 years to complete (*54*). Substantially after this event, an erosional channel formed between the talus cone and the western dolomite wall, also eroding the top of the GSS sediments in the Warthog Cave section. This erosional channel was filled with the WCFS that has been U-Pb dated to 1.789 ± 0.104 Ma old (DN09) (*21*) but whose age can be refined to between 1.89 and 1.78 Ma because of its normal polarity and correlation to the Olduvai Subchron (1.95 to 1.78 Ma old). The WCFS caps FBU2, although most of the fossil-bearing sediments in FBU2 only occur in the top ~90 cm of the Walls of Jericho and Italian Job pinnacles (Fig. 14) and were formed immediately after the reversal at ~1.95 Ma ago. Although a younger US-ESR age of 1.712 ± 0.538 Ma has been produced for a tooth from the Eurydice (DNH 7) block that may suggest deposition during FBU2, the ex situ nature of the block and its decalcification make dosimetry estimates more difficult. The Eurydice block consists of CSB and is consistent with deposition in FBU1, and the US-ESR age does overlap with the other ages from FBU1 within error. Moreover, comparisons between the ESR dating of teeth from calcified and decalcified breccia at other sites show that decalcification causes ages that are too young (*15*). As such, it is critical to collect teeth from in situ calcified breccia when undertaking US-ESR analysis at such sites. The lack of any short magnetic reversal events—such as the ~2.07-Ma-old Huckleberry Ridge event (*45*), identified at other palaeocaves in the region (*9*, *15*) within deposits older than the reversal at DMQ—suggests that the deposits all formed after ~2.07 Ma ago, which is consistent with the median age of the US-ESR sample from the Jangi buttress. The vast majority of hominin remains from DMQ, including DNH 134 and DNH 152, thus come from FBU1 maximally between 2.28 and 1.95 Ma ago but most likely between ~2.04 and 1.95 Ma ago.

Biogeographic interpretations of the DMQ faunas

There are several faunal species represented at DMQ (*32*) that support some level of non-endemic mammal dispersal into South African palaeoecosystems during the early Pleistocene and/or temporal variation within South African phyletic lineages. The recovery of *Equus* cf. *quagga* ssp. is consistent with the deposits having formed after ~2.3 Ma ago, given the first appearance of the genus in eastern Africa at this time (*32*). *Equus* is first seen in South Africa at Sterkfontein Member 4 before ~2.07 Ma ago (*6*, *15*), as well as at Malapa just after ~2 Ma ago (*9*). This indicates the relatively rapid expansion of this genus into the southern part of the continent, perhaps coinciding with environmental change and increasing aridity at this time (*27*).

The papionin sample at DMQ (DN 403, 528, 541, 2160, 2162, and 2344) is best attributed to *Papio robinsoni*. Diagnostic features include a prominent glabelar region, definitive anteorbital drop, definitive facial fossae, and a dorsally flattened rostrum with rounded maxillary ridges that are elevated superiorly to the nasal bones. They are distinct from *Papio hamadryas*, which is found at penecontemporary sites such as Malapa (*55*), by the aforementioned rostral morphology and rounder maxillary ridges and by having less excavated facial fossae. However, the specimens collectively share distinct facial fossae that depart from their conspecifics at Swartkrans Member 1. Specifically, the anterior extent of the maxillary fossae on the DMQ specimens are not as

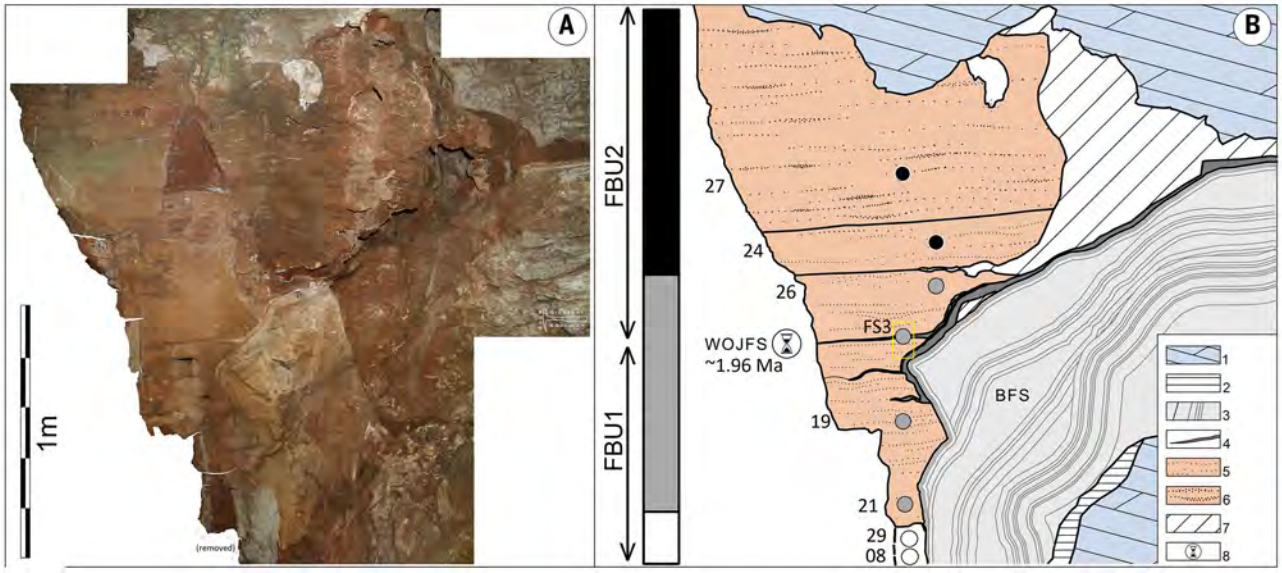

Fig. 10. Walls of Jericho pinnacle. (**A**) Photograph and (**B**) section showing stratigraphy, palaeomagnetic polarity, and geochronometric data. 1, dolomite bedrock; 2, wad and other dolomite weathering products; 3, BFS; 4, flowstone; 5, GSS, sandstone/siltstone; 6, GSS, coarse sandstone and fine gravel; 7, decalcified sediment; 8, WOJFS dated by means of U-Pb to 1.962 ± 0.107 Ma old. Palaeomagnetic data are indicated with black circles, normal polarity; gray circles, intermediate polarity; and white circles, reverse polarity. The yellow box shows the location of the micromorphology sample.

developed as the Swartkrans specimens SK 555, SK 557, and SK 560. The infraorbital region is not as excavated by the maxillary fossae in the DMQ specimens. As the malar root approaches the alveolar bone in the Swartkrans Member 1 material, it typically curves anteriorly (further defining the maxillary fossae) (*56*). However, in nearly every DMQ specimen, the malar root descends directly on the alveolar bone between the second and third molar. This variation may be explained by temporal variation between DMQ and Swartkrans Member 1, with the latter perhaps dating closer to 1.8 Ma ago (*5*). Other sites (such as Pit 23 at Bolt's Farm) that have definitively yielded *P. robinsoni* remain undated (*57*), making DMQ the earliest definitive evidence for this species (*56*).

The hunting hyaena *Lycyaenops* is first recorded in the early Pliocene of Europe as *Lycyaenops rhomboideae* (*58*) and appears by 3.85 to ~3.63 Ma ago as *Lycyaenops* cf. *silberbergi* in the Upper Laetolil Beds at Laetoli (*59*) and in South Africa at Sterkfontein Members 2 and 4 between 2.61 and 2.07 Ma ago (*6*, *21*). During this period, *Lycyaenops* cohabits the South African ecosystems with *Chasmaporthetes*, a genus present in South Africa at Langebaanweg by ~5.15 Ma ago (*60*, *61*). DMQ represents the last appearance of *Lycyaenops*, whereas the South African *Chasmaporthetes nitidula* persists into the early Pleistocene (*5*). This suggests that any environmental conditions favoring the initial dispersal of *Lycyaenops* into South Africa may not have existed after DMQ.

The oldest occurrence of *Dinofelis* (*D.* cf. *diastemata*) is in South Africa at Langebaanweg ~5.15 Ma ago (*61*, *62*). By the end of the Pliocene, *Dinofelis* is represented by *D. aronoki* in eastern Africa and *D. barlowi* and *D. darti* in South Africa (*62*). The only *Dinofelis* definitively known to be present in Africa after ~1.87 Ma is *D. piveteaui* (*62*), with *D. barlowi*

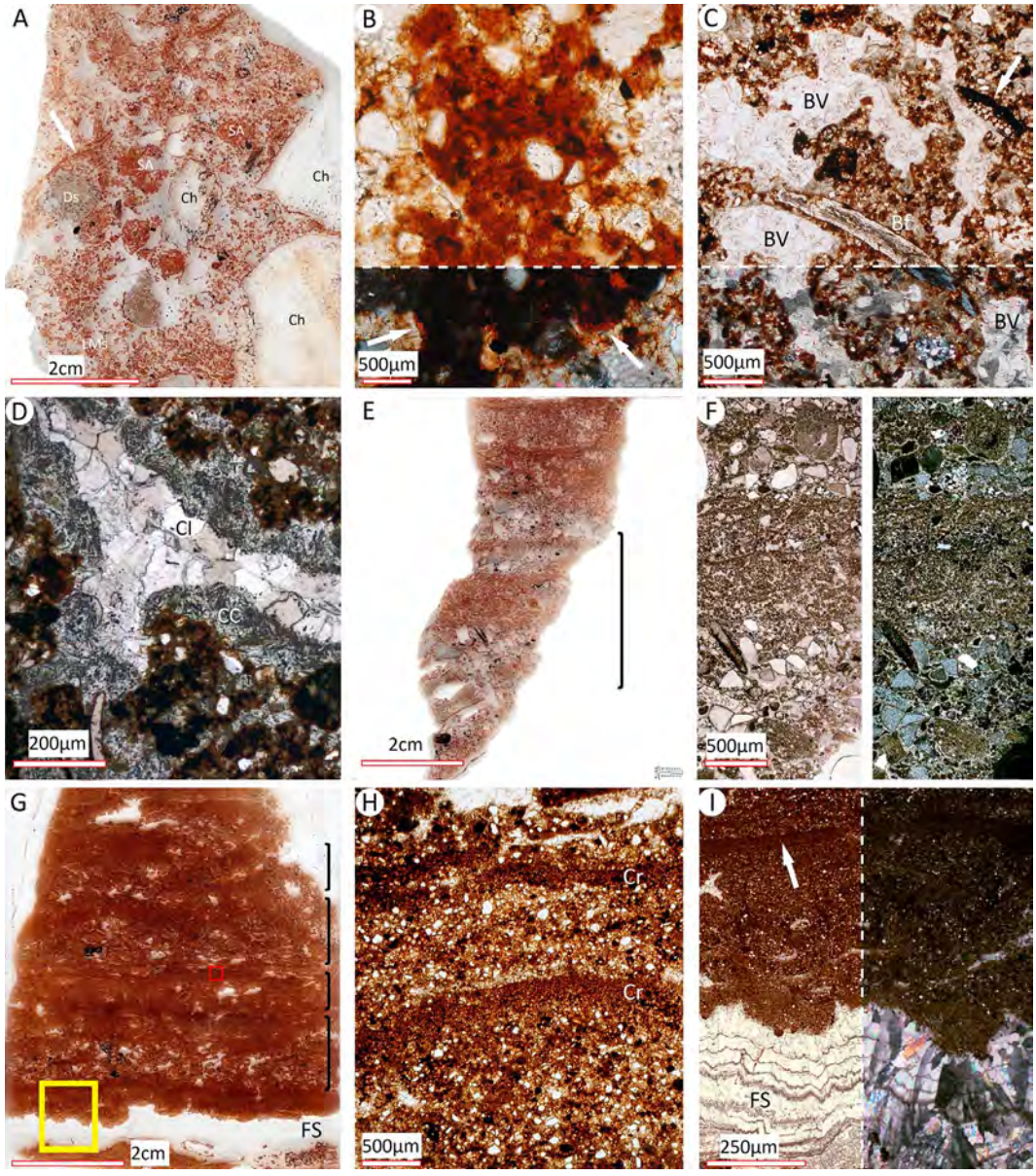

Fig. 11. Micromorphology of selected aspects of the DMQ infill. (**A**) High-resolution scan of thin section of CSB (main talus cone) sample MM26, from WW, showing loose microstructure (LMs), chert (Ch), and dolomite (Ds) clasts, reworked soil and sediment aggregates (SA), sometimes showing crust-like features probably reworked from sandstone and siltstone sediments. (**B**) CSB sample MM04 from WW, with clay aggregate stained by amorphous iron- and subordinately manganese-oxides. The bottom third is under crossed polarizers (XPL), showing poorly developed stipple-speckled b-fabric (white arrows) in unstained areas. (**C**) CSB sample MM01 from WC, with bone fragment (Bf), monocoth-like wood fragment (white arrow), wide pores originated by biological activity (BV). The bottom third of the panel is under XPL, showing anhedral sparite infills within pores. (**D**) Sample MM32 from WC. Void with "dusty" calcite coating (CC) probably derived from recrystallization of aragonite and subsequent sparitic anhedral calcite infilling (Cl). (**E**) High-resolution scan of thin section of MSB (intermediate facies) sample MM18L from Italian Job; sequence of fining-upwards sequences with centimeter-size clasts at the base of each sequence; the bracket highlights the sequence in (F). (**F**) Mosaic of microphotographs under plane polarized light (PPL) (left) and XPL (right), showing a fining upward sequence with thin clay crusts interbedded within the fine part. (**G**) High-resolution scan of thin section of GSS (distal facies) sample MM12 from WOJ (above WOJFS), with fine grainsize fining-upward sequences (black brackets), interbedded with a thin flowstone crust (FS); the red and yellow squares indicate respectively the areas in (H) and (I). (**H**) Very fine silt and clay crusts (Cr) topping fining upward sequences. (**I**) Columnar calcite flowstone (FS) with multiple short growth hiatus marked with detrital caps on crystal tips. The flowstone is overlain by a fining upward sequence terminated by a clay crust (white arrow). (Right) Under XPL.

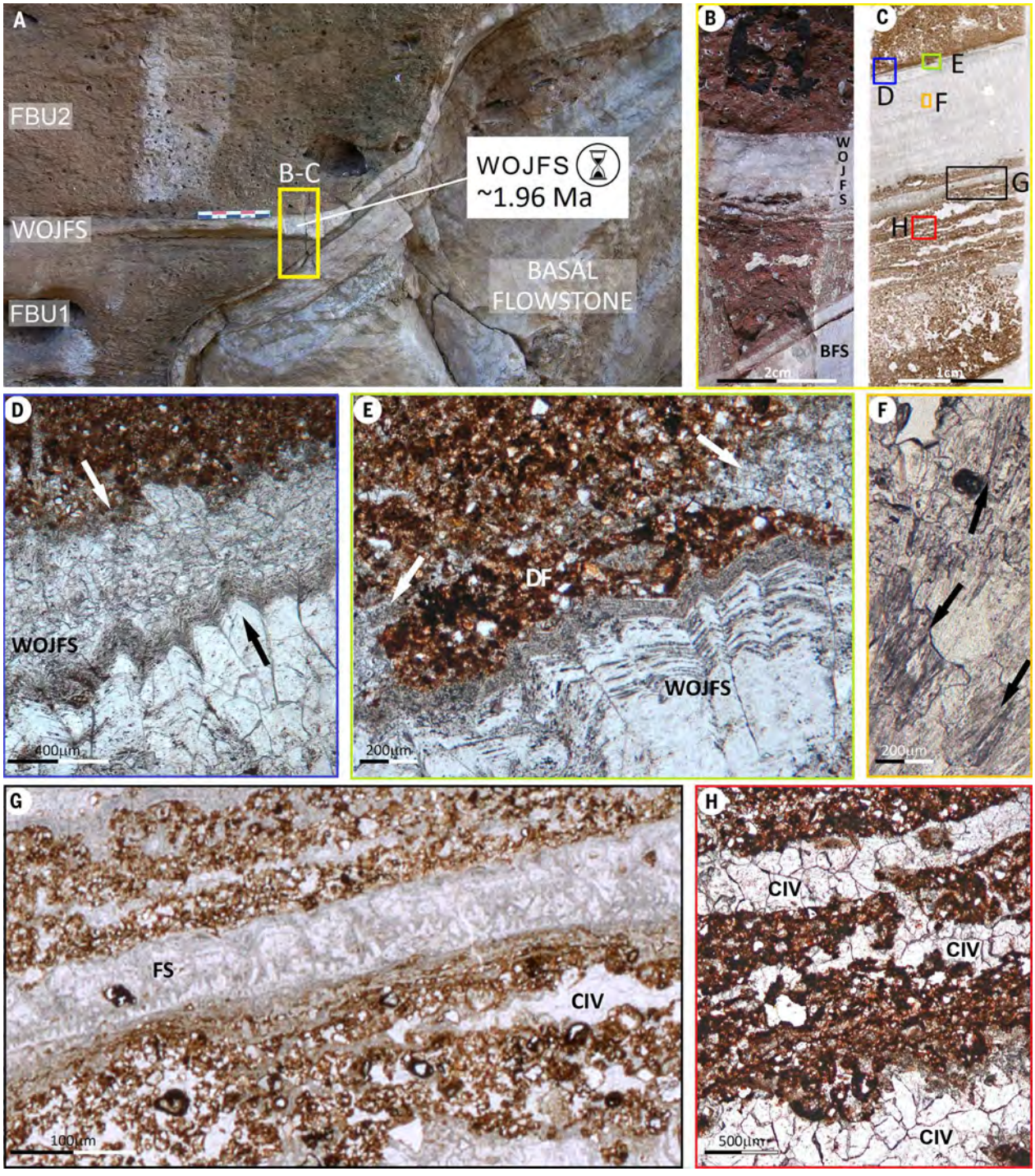

Fig. 12. Micromorphology of the WOJFS. (**A**) Aspect and stratigraphy of the ~1.95-Ma-old WOJFS, as in the northern side of the Walls of Jericho pinnacle, showing that WOJFS formed during a stop in clastic deposition and is not intrusive into GSS. FBU1 and FBU2, flowstone-bounded units 1 and 2 (Fig. 14). The yellow rectangle indicates micromorphology samples. Scale bar, 5 cm. (**B**) Short-range picture of the micromorphology sample detachment niche inside yellow rectangle of (A). BFS, basal flowstone. (**C**) Scan of thin section showing the distinct nature of sedimentation below and above WOJFS, with several fine speleothem crusts alternating with silt before the formation of the main flowstone. Colored rectangles indicate spots described in (D) blue; (E) green; (F) amber; (G) black; (H) red. (**D**) Top of WOJFS and upper contact (white arrow) with the overlying USS. Black arrow indicates subhedral sparitic calcite with rombohedron faces indicating upward crystal growth direction. The layer of anhedral calcite crystals between the arrows is recrystallized, and the top surface has undergone dissolution because of contact with siltstone. PPL, plane polarized light. (**E**) Same as in (D), showing a wide gulf-like dissolution feature (DF) into the upper surface of WOJFS layer, because of contact with subsequently deposited silt. White arrows indicate remains of the upper layer (PPL). (**F**) High magnification of calcite within WOJFS, showing the remnant needle-like aragonite (black arrows) that was critical to the successful dating of the sample by U-Pb (PPL). (**G**) Thin flowstone crust (FS) underlying the main WOJFS, showing preserved upward-growth pattern. Lens-like voids were subsequently infilled with anhedral calcite (CIV). (**H**) Precipitation of anhedral calcite spar (CIV) within channel voids.

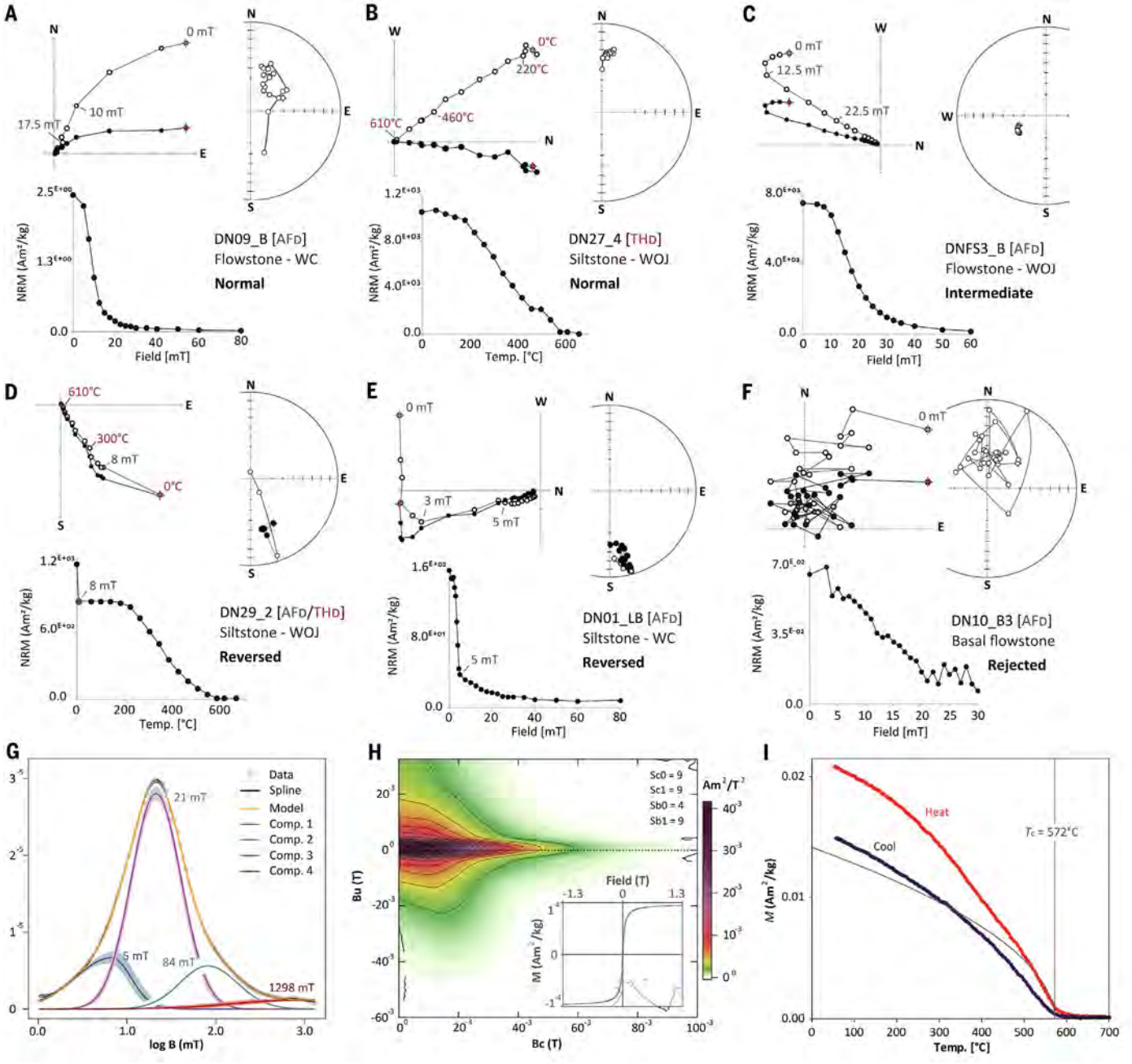

Fig. 13. Palaeomagnetic data from DMQ. (**A** to **F**) (Top) Representative palaeomagnetic data plots for DMQ (vector, stereographic, and demagnetization spectra). Open symbols on stereographic plots indicate negative inclination, and closed symbols indicate positive inclination. (Bottom) Mineral magnetic results for the DMQ. (A) DN09b normal polarity >2.61-Ma-old basal flowstone. (B) DN27 normal polarity siltstone from the top of the Walls of Jericho. (C) DNFS3 intermediate polarity ~1.95-Ma-old WOJFS. (D) DN29 reversed polarity siltstone from base of the Walls of Jericho. (E) DN01 reversed polarity siltstone from the Warthog Cave section. (F) DN10 rejected basal flowstone sample with normal trend but with MAD > 15. (**G**) Unmixed coercivity contributions to a representative backfield curve, with labeled remanence coercivities for each component (comp.). (**H**) FORC diagram, with smoothing parameters listed (for example, Sc0) and a hysteresis loop insert. (**I**) thermomagnetic curve with Curie temperature estimate.

last known to occur at Malapa and now DMQ at ~2 Ma ago (*9*, *32*). Moreover, *D. barlowi* and *Dinofelis* aff. *piveteaui* co-occur at DMQ (*29*), marking the first time that these taxa have been found together at the same site. Historically, *D. piveteaui* has been interpreted as being directly descended from *D. barlowi* (*62*–*64*), but Werdelin and Lewis (*62*) posited a close relationship between the eastern African *D. aronoki* and the later-occurring *D. piveteaui*. An ancestor-descendent relationship between *D. aronoki* and *D. piveteaui* suggests the expansion of a population of the east African *D. aronoki*, or a population transitional between *D. aronoki* and *D. piveteaui*, at some point just before 2.0 Ma ago. This population, possibly represented by the DMQ *Dinofelis* aff. *piveteaui* (*32*) and the Cooper's D *Dinofelis* sp. ~1.36 Ma ago (*21*, *65*), may have displaced the South African endemic *D. barlowi*.

The dominance of the antilopin *Antidorcas recki* in the DMQ deposits (28.6% of the total

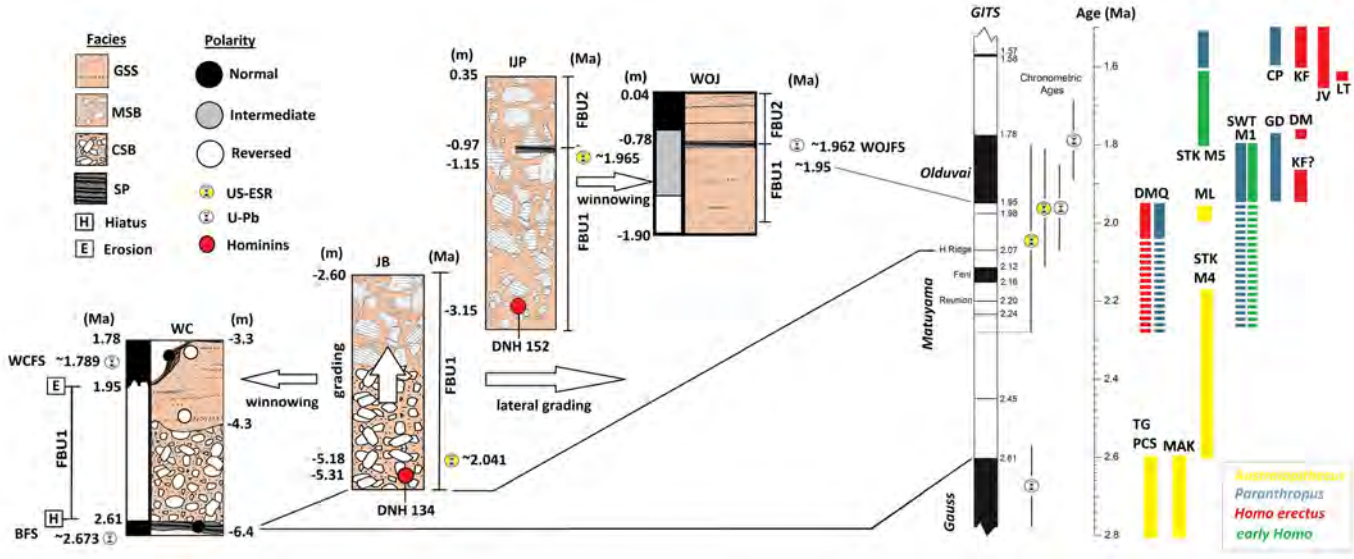

Fig. 14. Composite stratigraphy for DMQ. The stratigraphic sections and dates (million years ago) for DMQ compared against the Geomagnetic Polarity time scale and other early hominins in South Africa as well as global *H. erectus* sites. WC, Warthog Cave; JB, Jangi Buttress; IJP, Italian Job pinnacle; WOJ, Walls of Jericho; m, meters below or above datum.

bovid assemblage) (*32*) may reflect movement by an earlier Neogene mammal population from outside South Africa into the evolving palaeocommunities of the region during the earliest Pleistocene. The species is present in the 3.44-Ma-old Shungura Formation Member B and younger deposits across eastern Africa, ultimately becoming common in terminal Pliocene deposits such as the 2.66-Ma-old Upper Ndolyana Beds at Laetoli (*66*). By contrast, the first South African *A. recki* specimens were not recovered until the modest sample (NISP, 5; MNI, 3) identified from the Sterkfontein Member 4 assemblage that formed between 2.61 and 2.07 Ma ago (with at least some of that fauna post-dating 2.33 Ma ago owing to the occurrence of *Equus*) (*6*, *26*). The hypothesis that South African *A. recki* occurred only ~1 Ma after evolving in eastern Africa draws support from two potentially interrelated factors. First, *Antidorcas* is notably absent from the large Makapansgat Member 3 assemblage (3.03 to 2.61 Ma ago, with faunal deposition close to the end of that period) (*6*), in which the dominant antilopin and the second-most common bovid is *Gazella vanhoepeni* (NISP, 472; MNI, 55) (*23*, *66*, *67*). Despite this abundant representation in Member 3, and potential relationship to the Langebaanweg *Gazella* (5.15 Ma ago) (*67*) and extant *Gazella* species, *G. vanhoepeni* has not been definitively identified from the extremely sparse record of indeterminate *Gazella* from any subsequent early Pleistocene South African deposit (*23*, *66*, *68*–*70*). Second, shortly after *A. recki* first appears at Sterkfontein Member 4, there was an adaptive radiation of *Antidorcas* in South Africa into at least two additional species (the extinct *A. bondi* and extant *A. marsupialis*). Collectively, species of *Antidorcas* are frequently recovered from early- to mid-Pleistocene palaeokarstic deposits in the region and form substantial components of the Swartkrans, Kromdraai B, and Cooper's D faunal assemblages (*32*, *68*–*70*). The apparent turnover in representation of antilopin genera from *Gazella* to *Antidorcas* coupled with rapid speciation in the latter group is suggestive of exploitation of changing regional palaeoecosystems in which *Antidorcas* species adapted to the progressive expansion of xeric South African Pleistocene palaeohabitats.

Conclusions and impact

The geology of DMQ further highlights the inadequacies of the Member system still used at other South African sites (*11*–*14*). As DMQ and other sites show (*6*, *19*–*20*, *70*), these different lithologic units can form synchronously, and wherever a siltstone and sandstone unit occurs, there is (or was) likely a paired breccia from which it was winnowed. The alternative, allostratigraphic criterion we used disentangles lithostratigraphy from chronology. The context and dating of the DNH 134 *H.* aff. *erectus* cranium and *P. robustus* fossils to between ~2.04 and 1.95 Ma ago show how DMQ is now one of the best dated sites in South Africa, as well as how the integration of geomorphology, stratigraphy, and high-precision age determinations are resolving the South African fossil karstic record and providing critical insights into hominin evolution.

Australopithecus is last known to occur ~2 Ma ago at Malapa (*2*, *9*) and perhaps as late as 2.07 Ma ago at Sterkfontein (*6*). *Australopithecus* thus persisted in southern Africa for roughly half a million years after it went extinct in eastern Africa (*50*). However, the precise timing of the first occurrence of *Homo* and *Paranthropus*, and whether it overlapped with *Australopithecus*, has been hard to resolve because of uncertainty in the depositional ages of fossils from Sterkfontein, Kromdraai B, and Swartkrans (somewhere between 2.3 and 1.8 Ma ago). At >1.95 Ma ago, the DNH 152 cranium represents the oldest confirmed representative of *P. robustus* in South Africa (Fig. 4). The age and association of the Kromdraai B *Paranthropus* fossils are presently unknown, although preliminary palaeomagnetic analysis indicated an age of <1.78 Ma for the hominin-bearing Member 3 deposits (*5*), and thus younger than DMQ. Although the *Paranthropus* fossils from the Swartkrans Member 1 Hanging Remnant have been dated to sometime between ~2.3 and 1.8 Ma ago (*5*, *21*), there is no firm evidence that they are >1.95 Ma old (*5*). A number of studies have suggested that the deposits are likely closer in age to the upper flowstone that was dated at 1.8 Ma ago, which is consistent with ESR dates (*71*) and faunal interpretations (*72*), including the difference noted between *P. robinsoni* at DMQ and Swartkrans Member 1 (*5*, *72*).

At ~2.04 Ma ago (minimum age 1.95 Ma), DNH 134 is the most complete and oldest early Pleistocene *Homo* neurocranium in South Africa (Fig. 1). DNH 134 is at least 100,000 to 150,000 years older than *H. erectus s.l.* specimens from Dmanisi (*73*) and over 300,000 years older than the KNM-ER-3733 cranium from Kenya at ~1.63 Ma old (*74*). The KNM-ER-2598 occipital fragment from eastern Africa shows affinities to *H. erectus* (*75*). However, on the basis of palaeomagnetic data, its location 4 m below

the KBS tuff (dated to 1.87 ± 0.02 Ma ago) would place KNM-ER 2598 within the Olduvai Subchron at <1.95 Ma ago (*76*–*78*). As such, DNH 134 represents the oldest fossil with affinities to *H. erectus* in the world. Despite this, we do not assert that the species necessarily evolved first in southern Africa, especially given major geological biases in hominin finds across Africa. However, the dating of the DNH 134 cranium to >1.95 Ma ago substantially weakens the hypothesis that *H. erectus sensu lato* evolved outside of Africa (*73*).

It has been postulated that *A. sediba* is a good candidate for the ancestor of *Homo* (*2*), although much older fossils attributed to *Homo* exist (*8*). *A. sediba* can only be ancestral to *Homo* in southern Africa if a population existed before DNH 134, for which there is no current evidence (*7*). An alternative scenario is that the *Homo*-like morphological elements in *A. sediba* (*2*) may instead represent homoplasy, evolved as local environmental pressures gave rise to convergent morphological features at ~2.0 Ma ago in a terminal population derived from *A. africanus* (*79*). Regardless, changing environmental conditions across Africa likely placed *Australopithecus* populations under selective pressures that led eventually to the evolution of divergent *Homo* and *Paranthropus* lineages (*80*, *81*).

Global climatic transitions have been suggested to occur at 3.0 to 2.5 Ma ago (with rapid global cooling and African landscape aridification) and 2.0 to 1.5 Ma ago (with the inception of the Walker Circulation in the Pacific governing tropical airflow and rainfall patterns across the continent) (*29*, *82*). Evidence for a major environmental shift in at least parts of southern Africa comes from deep-sea cores off Namibia, which indicate stronger climatically induced fluctuations between 2.7 and 2.2 Ma ago, with semi-arid environments more widespread during glacial periods (*27*). Aridification and climate variability further increased substantially after 2.2 Ma ago (*27*), although humid conditions occurred in the Limpopo basin between 2.0 and 1.75 Ma ago (*28*). These climatic shifts are shown in the caves by changes from major phases of massive speleothem and tufa deposition in the Pliocene at the Makapansgat Limeworks and Taung (*6*) to increasingly sporadic formation throughout the Pleistocene (*21*). Some researchers have suggested that hominin evolution has been driven by long-term trends toward aridity (*83*), whereas others suggest the importance of short periods of extreme climatic change or variability (*84*). When set within the regional record, the DMQ sequence highlights that although an overall trend toward aridity occurred, the period between 2.3 and 2.0 Ma ago was a critical period of major ecological change and dispersal that extensively modified South African faunal communities.

The changes seen in hominin taxa are mirrored in other fauna, with DMQ representing a transitional faunal community overlapping between older, >2.1-Ma-old sites such as Sterkfontein Member 4 and Makapansgat Limeworks Member 3 (*6*) and younger sites such as Swartkrans and Gondolin (*5*). The transitional faunal community recorded at DMQ reflects the larger turnover in mammal communities driven by major ecological changes in southern Africa that saw the extinction of South African endemic species, dispersal of new species, and adaptive radiation in the region. This suggests that South Africa was a center for the evolution of mammalian lineages as well as a refuge for ancient lineages in the early Pleistocene. The high taxonomic diversity on the South African landscape around 2 Ma ago is likely a response of indigenous hominins and other fauna to climate and environmental shifts, in tandem with new immigrants that were part of a series of radiations across Africa that set the stage for hominins leaving the continent and inhabiting Asia sometime between 2.12 and 1.95 Ma ago (*85*). We interpret the occurrence of *Homo* aff. *erectus* at this time in South Africa, and soon after at Dmanisi (*73*), as evidence for a major range expansion of this species (covering at least 8000 km) both out of and within Africa around 2.0 to 1.8 Ma ago.

At ~2.04 to 1.95 Ma ago, DMQ records a critically underrepresented time period in the evolution of South African faunas and palaeoecosystems and shows unequivocally that *A. sediba* (from Malapa at ~1.98 Ma ago) (*2*, *9*), *P. robustus*, and *Homo* aff. *erectus* occurred contemporaneously within the ~250 km^2 of karst landscape northeast of Johannesburg, even though it cannot be demonstrated definitively that they were truly sympatric. With the last occurrence of *A. africanus* (Sts 5) potentially as late as ~2.07 Ma ago at Sterkfontein Member 4, the South African record has a very high diversity of hominins at ~2.1 to 1.9 Ma ago (*5*, *6*). We suggest that southern Africa served as an ecological refugium for *Australopithecus* until just after 2.0 Ma ago, when either short- or long-term climatic variability would have finally driven *Australopithecus* to extinction. It is unclear whether biological or behavioral adaptations in *Australopithecus* (*80*) or competition with *Homo* and/or *Paranthropus* would have also contributed to the demise of the genus, but the dating of DNH 134 and DNH 152 to a period of overlap with *Australopithecus* now make this a possibility.

Materials and methods

Reconstruction of endocranial volume

Based on surface scans of the original fossil, acquired through use of the Artec Spider scanner following methodology outlined in Adams *et al.* (*86*), we extracted the preserved endocranial surface of DNH 134 and generated a partial virtual endocast by smoothly filling in missing regions. We used a symmetric human template of an endocranial landmark configuration (935 landmarks and sliding semilandmarks) (Fig. 3) (*87*–*88*), and defined which landmarks and sliding semilandmarks are preserved and which are missing. Semilandmarks were slid to the symmetric template configuration to gain point-to-point correspondence between individuals using the bending energy of the thin-plate-spline algorithm as a minimization criterion. Endocranial (semi)landmarks were also captured for an extant reference sample including 90 humans, 27 chimps, 39 gorillas and 44 orangutans, as well as for four African and four Asian *H. erectus* individuals (KNM-ER-3733, KNM-ER-3883, KNM-WT-15000, OH9, Sambungmacan 3, Sangiran 2, Ngandong 14, and Nwagi) (*89*).

On the basis of the extant reference sample, a multiple linear regression model was established to estimate endocranial volume from the endocranial form of the preserved regions of DNH 134 as captured from the landmarks (*89*). Pretending that the same regions as in DNH 134 are missing in each of the reference individuals as well as the listed *H. erectus* individuals and using the same methodology to estimate their endocranial volume allows comparison of the estimated and actual endocranial volume and therefore an interpretation of how the choice of the reference sample influences the estimates (*89*–*90*). This analysis (Fig. 3) shows that predicted and actual endocranial volumes are highly correlated without a taxon-dependent bias toward over- or underestimation so that DNH 134's endocranial volume can be estimated reliably.

Additionally, the missing portions of DNH 134's endocranial surface were reconstructed based on thin-plate-spline warping of the extant reference sample and the reconstructions' endocranial volumes were measured. The average or most common value and the range of estimates based on different reference individuals can be interpreted as the most probable value and estimation uncertainty, respectively (*90*, *91*). Assuming that the same regions as in DNH 134 are missing in each of the reference individuals as well as the listed *H. erectus* individuals, we estimated their endocranial volumes as well and compared them to their measured cranial capacities (Fig. 3). If the pooled reference sample including humans and apes is used, the endocranial volume of smaller individuals (apes) is predicted too small. A good estimate is possible if the "correct" reference sample (the same species) was used (Fig. 3). Using humans and apes in a pooled reference sample to reconstruct DNH 134 might therefore lead to (slight) over- or underestimation of its endocranial volume. However, our results show that endocranial volume estimates based on thin-plate spline reconstructions (484 to 593 cm^3) are consistent with regression-based estimates (514 to 564 cm^3).

As a 2-to-3-year-old individual, DNH 134 had not reached its adult brain size when it died, although it was likely approaching the adult population range of variation. We computed Gompertz growth curves for ontogenetic data of human and chimpanzee data from the literature for comparison (*87*, *92*–*97*). A 2-year-old individual with a cranial capacity of 538 cm^3 would grow into an adult of 661 cm^3 and 577 cm^3 according to the human and the chimpanzee growth curve, respectively, while a three-year-old individual would grow into an adult of 588 cm^3 and 551, respectively. Despite its juvenile status, we therefore suggest that DNH 134 documents small brain size in this population.

Stratigraphy and micromorphology

The characteristics of the sediments were observed and described on natural profiles (dissolution shapes), old quarry cuts, and recent excavation profiles and surfaces. Descriptions were carried out following Catt (*98*). Emphasis was given to texture, boundaries, sedimentary structures and, more generally, to the architecture of the sedimentary bodies, to reconstruct the stratigraphy of the cave infill. Litho- and allostratigraphic units (*99*) were used in assessing the stratigraphic sequence and then lumped into chronostratigraphic Flowstone Bound Units (*22*). Texture data were inferred from field observations and the measurement of clasts in exposed profiles, on freshly broken sections of hand samples, and from micromorphological samples in thin section under polarising microscope. Micromorphological observations were carried out on undisturbed sediment samples. Oriented blocklets were detached from natural or excavation profiles; their coordinates were recorded by a total station, and by far-field and macrophotography. The samples were air-dried in laboratory at 35°C in ventilated oven, and impregnated, including the cemented samples, by epoxy resin under medium vacuum and let polymerise. The resulting samples were cut by diamond saw, polished, glued on 90- by 60-mm or 60- by 45-mm microscope slides and ground to 30 μm on abrasive disks, using petroleum for lubrication. The resulting slides were protected by standard cover slides and labeled. Observations were carried out following the standard formalised by Bullock *et al.* (*100*) and Stoops (*44*). Thirty-eight monoliths were collected from locations selected to represent the most relevant aspects of the various lithologic units, as well as local peculiarities.

Coupled US-ESR

For each tooth a small fragment of dentine and enamel was removed using a hand-held saw, with a 300-μm-thick diamond blade. The small fragment was then cut in half exposing a flat surface of dentine and enamel for U-series analyses. Internal dose rate was calculated using U-series values obtained by means of laser ablation multicollector inductively coupled plasma mass spectrometry (LA-MC-ICPMS) on a Thermo Neptune plus coupled to ESI NW193 and ICPMS quadrupole Agilent 7700 for concentration correction of ^{238}U. The values measured in the enamel and the dentine, are consistent across the measured area. An average value was calculated for each dental tissue and used for the US-ESR model. Baseline and drift were corrected using a NIST 612 glass disc, while a fossil hippopotamus tooth of known U-series concentration was used to correct $^{234}U/^{238}U$ and $^{230}U/^{238}U$ ratios and assess the accuracy of measurements. Concentrations obtained by LA-MC-ICPMS were compared to quadrupole ICPMS analyses on the same dentine and enamel fragments (table S2). To account for tailing effects, measurements were carried out at half-masses of 229.5 and 230.5 for ^{230}Th and 233.5 and 234.5 for ^{234}U. The other half was used for ESR measurements, by separating the different dental tissues. Both DMQ-2 and DMQ-3 enamel fragments removed from each sample and used for the ESR measurements were directly in contact with the dentine on one side and directly in contact with the sediment on the other side (no cement). The outer surface of the enamel (in contact with the surrounding sediment) and the dentine directly attached to it were removed using a diamond blade rotary tool. Simultaneously, 100 μm on each side was removed to avoid alpha particle contribution.

ESR dating for Drimolen fossil teeth was performed on a Freiberg MS5000 X-band spectrometer at 1 G modulation amplitude, 2 mW power, 100G sweep, and 100 kHz modulation frequency, coupled to a Freiberg x-ray irradiation chamber, which contains a Varian VF50 x-ray gun at a voltage of 40 kV and 0.5 mA current. Each tooth fragment was mounted onto a teflon sample holder, allowing the fragment to be exposed directly to the x-ray source with no shielding (except for a 200μm aluminum cover). To estimate the ESR equivalent dose (D_e), each fragment was irradiated nine times, following exponentially increasing irradiation times [90, 380, 1080, 1800, 3600, 7200, 14,700, 28,800, and 63300 s, with an average dose rate for DMQ-2 and DMQ-3 of 0.22 grays (Gy)/s 0.25 Gy/s respectively]. The x-ray emission received by the bovid teeth was calibrated using added known gamma irradiation dose performed at the Australia's Nuclear Science and Technology Organisation (ANSTO). During each irradiation step, the output of the x-ray gun was recorded, to allow an accurate determination of the dose received by the sample at each irradiation steps. Fitting procedures were carried out with the *McDoseE 2.0* software that uses a Bayesian framework approach, where the solution is a full probability distribution on the dose equivalent (*101*). The dose response curves (DRCs) were obtained by averaging the peak-to-peak T_1-B_2 ESR intensities recorded for each irradiation dose over 180° (10° step) measurements and merged into a single spectrum (*47*). Isotropic and baseline corrections were applied uniformly across the measured spectra (*48*). The final D_E values were obtained by fitting a single saturating exponential (SSE) through the ESR intensities and by selecting the appropriate maximum irradiation dose (D_{max}) in order to avoid dose estimation inaccuracy (*102*).

The external dose rate (table S3) was calculated using the U, Th, and K content of sediment collected from the site as well as measured directly using a portable gamma-spectrometer Inspector 1000. Measurements were made in places were breccia was already fractured. Some results where the probe could not be fully surrounded by 30 cm of sediment were modeled using the sedimentary geometric configuration around the probe (*Modeled breccia*), but represent poorly constraint measurements and were therefore removed from calculation. The Drimolen cosmic dose rate was estimated, considering the site variation over the burial time as detailed in this study. With an estimated cover of about 30m of dolomite (using 2.85 ± 0.03 g cm^{-3} average density value) in the original context and a gradual denudation rate of 10 m per million years. The large error takes into consideration sudden collapse of parts of the dolomite instead of a gradual denudation rate (table S3).

Palaeomagnetism

A series of 12 independently oriented samples (Table 1) were taken from the Drimolen palaeocave deposits targeting clastic siltstone sequences and flowstones. These were taken as block samples and were oriented in situ using a Suunto magnetic compass and clinometer. Subsequent corrections were made for the local dip of the stratigraphy and the declination of the local field according to the International Geomagnetic Reference Field (IGRF), accessed through the British Geological Survey (www.geomag.bgs.ac.uk/data_service/models_compass/igrf_form.shtml). Block samples were drilled and cut into standard 20- by 25-mm palaeomagnetic subsamples using water-cooled preparation equipment. Palaeomagnetic experiments were undertaken at The Australian Archeomagnetism Laboratory (TAAL), with additional mineral magnetic tests performed at the University of Liverpool Geomagnetism Laboratory (ULGL; UK) and Institute for Rock Magnetism (IFRM), University of Minnesota (USA). Mass specific magnetic susceptibility measurements at low (χLF) and high (χHF) frequency were undertaken using a Bartington MS3 system for frequency-dependant, room-temperature analysis. Isothermal remanent magnetization (IRM) acquisition curves and backfields, hysteresis loops and M/T were run

on a magnetic measurements variable field translation balance (VFTB) at ULGL, with additional IRMs imparted by using a MMPM10 pulse magnetizer at TAAL. Curie temperatures (T_c) were calculated from M/T heating curves using the Moskowitz *et al.* protocol (*103*) smoothed with a 3-point running average in RockMagAnalyizer 1.1 (*104*). First-order reversal curves (FORCs) were measured on a Princetown micromag vibrating sample magnetometer at IFRM and processed by using FORCinel 3.0 (*105*) and VARIFORC smoothing (*106*). Hysteresis backfield curves were deconvoluted using MAX UnMix (*107*). Palaeomagnetic samples primarily underwent a 16-point TH_D using a shielded Magnetic Measurements MMTD80a Thermal Demagnetiser in a zero-field cage. AF_D was also undertaken for comparative purposes using a Molespin alternating field demagnetiser and an Advanced Geoscience Instruments Company (AGICO) LDA5 alternating field demagnetizer. An additional hybrid demagnetisation strategy was used incorporating low field AF_D steps (for example, to 8 to 12 mT) before standard TH_D which has shown to be useful in removing viscous overprints in palaeokarst deposits (*9*, *18*, *19*). All remanence measurements were made using an AGICO JR6 spinner magnetometer at TAAL. Subsample ChRM directions were isolated by using principle component analysis (*108*) and were accepted with MAD of <15°. Final directions for each block sample were calculated from between three and seven subsample ChRMs using Fisher (*109*) statistics. Polarity directions were assigned based on virtual geomagnetic pole latitudes of +90 to +60 (normal), +60 to −60 (intermediate), and −60 to −90 (reversed).

REFERENCES AND NOTES

1. A. W. Keyser, The Drimolen skull: The most complete Australopithecine cranium and mandible to date. *S. Afr. J. Sci.* **96**, 189–193 (2000).
2. L. R. Berger *et al.*, *Australopithecus sediba*: A new species of *Homo*-like australopith from South Africa. *Science* **328**, 195–204 (2010). doi: 10.1126/science.1184944; pmid: 20378811
3. D. S. Strait, B. A. Wood, Early hominid biogeography. *Proc. Natl. Acad. Sci. U.S.A.* **96**, 9196–9200 (1999). doi: 10.1073/pnas.96.16.9196; pmid: 10430919
4. D. Curnoe, A review of early *Homo* in southern Africa focusing on cranial, mandibular and dental remains, with the description of a new species (*Homo gautengensis* sp. nov.). *Homo* **61**, 151–177 (2010). doi: 10.1016/j.jchb.2010.04.002; pmid: 20466364
5. A. I. R. Herries, J. W. Adams, Clarifying the context, dating and age range of the Gondolin hominins and *Paranthropus* in South Africa. *J. Hum. Evol.* **65**, 676–681 (2013). doi: 10.1016/j.jhevol.2013.06.007; pmid: 23911292
6. A. I. R. Herries *et al.*, in *Palaeobiology of* Australopithecus, *Vertebrate Palaeobiology and Palaeoanthropology series*, K. E. Reed, J. G. Fleagle, R. Leakey, Eds. (Springer, 2013) pp. 21–40.
7. B. Villmoare *et al.*, Early *Homo* at 2.8 Ma from Ledi-Geraru, Afar, Ethiopia. *Science* **347**, 1352–1355 (2015). doi: 10.1126/science.aaa1343; pmid: 25739410
8. L. R. Berger *et al.*, *Homo naledi*, a new species of the genus *Homo* from the Dinaledi Chamber, South Africa. *eLife* **4**, e09560 (2015). doi: 10.7554/eLife.09560; pmid: 26354291
9. P. H. D. M. Dirks *et al.*, Geological setting and age of *Australopithecus sediba* from southern Africa. *Science* **328**, 205–208 (2010). doi: 10.1126/science.1184950; pmid: 20378812
10. A. B. Leece *et al.*, The first hominin from the early Pleistocene paleocave of Haasgat, South Africa. *PeerJ* **4**, e2024 (2016). doi: 10.7717/peerj.2024; pmid: 27190720
11. K. Butzer, Lithostratigraphy of the Swartkrans formation. *S. Afr. J. Sci.* **72**, 136–141 (1976).
12. C. K. Brain, A re-interpretation of the Swartkrans site and it remains. *S. Afr. J. Sci.* **72**, 141–146 (1976).
13. T. C. Partridge, Hominid-bearing cave and tufa deposits, in *The Cenozoic in Southern Africa*, T. C. Partridge, P. R. Maud, Eds. (Oxford Univ. Press, 2000), pp. 100–125.
14. L. Bruxelles, R. Maire, R. Couzens, J. F. Thackeray, J. Braga, A revised stratigraphy of Kromdraai, in *Kromdraai: a Birthplace of Paranthropus in the Cradle of Humankind*, J. Braga, J. F. Thackeray, Eds. (Sun Press, 2016), pp. 31–48.
15. A. I. R. Herries, J. Shaw, Palaeomagnetic analysis of the Sterkfontein palaeocave deposits: Implications for the age of the hominin fossils and stone tool industries. *J. Hum. Evol.* **60**, 523–539 (2011). doi: 10.1016/j.jhevol.2010.09.001; pmid: 21392817
16. D. Stratford, L. Bruxelles, R. J. Clarke, K. Kuman, New stratigraphic interpretations of the fossil and artefacts-bearing deposits of the Name Chamber, Sterkfontein. *S. Afr. Archaeol. Bull.* **67**, 159–167 (2012).
17. L. Bruxelles *et al.*, A multiscale stratigraphic investigation of the context of StW 573 'Little Foot' and Member 2, Sterkfontein Caves, South Africa. *J. Hum. Evol.* **133**, 78–98 (2019). doi: 10.1016/j.jhevol.2019.05.008; pmid: 31358185
18. J. W. Adams, A. I. R. Herries, K. L. Kuykendall, G. C. Conroy, Taphonomy of a South African cave: Geological and hydrological influences on the GD 1 fossil assemblage at Gondolin, a Plio-Pleistocene palaeocave system in the Northwest Province, South Africa. *Quat. Sci. Rev.* **26**, 2526–2543 (2007). doi: 10.1016/j.quascirev.2007.05.006
19. A. I. R. Herries *et al.*, Geoarchaeological and 3D visualisation approaches for contextualising in situ fossil bearing palaeokarst in South Africa: A case study from the ~2.61 Ma Drimolen Makondo. *Quat. Int.* **483**, 90–110 (2018). doi: 10.1016/j.quaint.2018.01.001
20. A. G. Latham, A. Herries, P. Quinney, A. Sinclair, K. Kuykendall, The Makapansgat Australopithecine Site from a Speleological Perspective, in *Geoarchaeology: Exploration, Environments, Resources*, A. M. Pollard, Ed. (Royal Geological Society, 1999), vol. 165, pp. 61–77.
21. R. Pickering *et al.*, U-Pb-dated flowstones restrict South African early hominin record to dry climate phases. *Nature* **565**, 226–229 (2019). doi: 10.1038/s41586-018-0711-0; pmid: 30464348
22. R. Pickering *et al.*, Stratigraphy, U-Th chronology, and paleoenvironments at Gladysvale Cave: Insights into the climatic control of South African hominin-bearing cave deposits. *J. Hum. Evol.* **53**, 602–619 (2007). doi: 10.1016/j.jhevol.2007.02.005; pmid: 17920104
23. R. J. Gibbon *et al.*, Cosmogenic nuclide burial dating of hominin-bearing Pleistocene cave deposits at Swartkrans, South Africa. *Quat. Geochronol.* **24**, 10–15 (2014). doi: 10.1016/j.quageo.2014.07.004
24. R. Stammers, M. Caruana, A. I. R. Herries, The first bone tools from Kromdraai and stone tools from Drimolen, and the place of bone tools in the South African Earlier Stone Age. *Quat. Int.* **495**, 87–101 (2018). doi: 10.1016/j.quaint.2018.04.026
25. L. Backwell, F. d'Errico, F. Early hominid bone tools from Drimolen, South Africa. *J. Archaeol. Sci.* **35**, 2880–2894 (2008). doi: 10.1016/j.jas.2008.05.017
26. E. Vrba, The fossil record of African antelopes (Mammalia, Bovidae) in relation to human evolution and palaeoclimate, in *Palaeoclimate and evolution with emphasis on human origins*, E. Vrba, G. Denton, T. Partridge, L. Burckle, Eds. (Yale Univ. Press, 1995), pp. 385–425.
27. L. M. Dupont, B. Donner, L. Vidal, E. M. Perez, G. Wefer, Linking desert evolution and coastal upwelling: Pliocene climate change in Namibia. *Geology* **33**, 461–464 (2005). doi: 10.1130/G21401.1
28. T. Caley *et al.*, A two-million-year-long hydroclimatic context for hominin evolution in southeastern Africa. *Nature* **560**, 76–79 (2018). doi: 10.1038/s41586-018-0309-6; pmid: 29988081
29. P. J. Hopley *et al.*, Orbital forcing and the spread of C4 grasses in the late Neogene: Stable isotope evidence from South African speleothems. *J. Hum. Evol.* **53**, 620–634 (2007). doi: 10.1016/j.jhevol.2007.03.007; pmid: 17942141
30. A. W. Keyser, C. G. Menter, J. Moggi-Cecchi, T. R. Pickering, L. R. Berger, Drimolen: A new hominid-bearing site in Gauteng, South Africa. *S. Afr. J. Sci.* **96**, 193–197 (2000).
31. J. Moggi-Cecchi, C. Menter, S. Boccone, A. Keyser, Early hominin dental remains from the Plio-Pleistocene site of Drimolen, South Africa. *J. Hum. Evol.* **58**, 374–405 (2010). doi: 10.1016/j.jhevol.2010.01.006; pmid: 20362324
32. J. W. Adams, D. S. Rovinsky, A. I. R. Herries, C. G. Menter, Macromammalian faunas, biochronology and palaeoecology of the early Pleistocene Main Quarry hominin-bearing deposits of the Drimolen Palaeocave System, South Africa. *PeerJ* **4**, e1941 (2016). doi: 10.7717/peerj.1941; pmid: 27114884
33. M. Bajwa *et al.*, Normal fusion of the metopic suture. *J. Craniofac. Surg.* **24**, 1201–1205 (2013). doi: 10.1097/SCS.0b013e31829975c6; pmid: 23851769
34. J. Pindrik, X. Ye, B. G. Ji, C. Pendleton, E. S. Ahn, Anterior fontanelle closure and size in full-term children based on head computed tomography. *Clin. Pediatr.* **53**, 1149–1157 (2014). doi: 10.1177/0009922814538492; pmid: 24920348
35. H. Coqueugniot, J.-J. Hublin, F. Veillon, F. Houët, T. Jacob, Early brain growth in *Homo erectus* and implications for cognitive ability. *Nature* **431**, 299–302 (2004). doi: 10.1038/nature02852; pmid: 15372030
36. S. C. Antón, Developmental age and taxonomic affinity of the Mojokerto child, Java, Indonesia. *Am. J. Phys. Anthropol.* **102**, 497–514 (1997). doi: 10.1002/(SICI)1096-8644(199704)102:4<497::AID-AJPA6>3.0.CO;2-P; pmid: 9140541
37. A. Balzeau, D. Grimaud-Hervé, T. Jacob, Internal cranial features of the Mojokerto child fossil (East Java, Indonesia). *J. Hum. Evol.* **48**, 535–553 (2005). doi: 10.1016/j.jhevol.2005.01.002; pmid: 15927659
38. S. C. Antón, Natural history of *Homo erectus*. *Am. J. Phys. Anthropol.* **122** (suppl. 37), 126–170 (2003). doi: 10.1002/ajpa.10399; pmid: 14666536
39. R. L. Holloway, D. C. Broadfield, M. S. Yuan, Brain endocasts, in *The Human Fossil Record*, (Wiley, 2004), vol. 3.
40. S. Benazzi, G. Gruppioni, D. S. Strait, J.-J. Hublin, Technical note: Virtual reconstruction of KNM-ER 1813 *Homo habilis* cranium. *Am. J. Phys. Anthropol.* **153**, 154–160 (2014). doi: 10.1002/ajpa.22376; pmid: 24318950
41. D. Falk *et al.*, The brain of LB1, *Homo floresiensis*. *Science* **308**, 242–245 (2005). doi: 10.1126/science.1109727; pmid: 15749690
42. C. K. Brain, The Transvaal Ape-Man-Bearing Cave Deposits: An overview of the sites at Sterkfontein, Kromdraai, Swartkrans and Makapan. *Transvaal Museum Memoir* no. 11 (1958).
43. A. I. R. Herries *et al.*, Integrating palaeocaves into palaeolandscapes: An analysis of cave levels and karstification history across the Gauteng Malmani dolomite. South Africa. *Quat. Sci. Rev.* **220**, 310–334 (2019). doi: 10.1016/j.quascirev.2017.02.007
44. G. Stoops, *Guidelines for Analysis and Description of Soil and Regolith Thin Sections* (SSSA, 2003).
45. B. S. Singer, A quaternary geomagnetic instability time scale. *Quat. Geochronol.* **21**, 29–52 (2014). doi: 10.1016/j.quageo.2013.10.003
46. T. A. Rivera, T. Darata, P. C. Lippert, B. R. Jicha, M. D. Schmitz, The duration of a Yellowstone super-eruption cycle and implications for the age of the Olduvai subchron. *Earth Planet. Sci. Lett.* **479**, 377–386 (2017). doi: 10.1016/j.epsl.2017.08.027
47. R. Joannes-Boyau, Detailed protocol for an accurate non-destructive direct dating of tooth enamel fragment using electron spin resonance. *Geochronometria* **40**, 322–333 (2013). doi: 10.2478/s13386-013-0132-7
48. R. Joannes-Boyau, R. A. Grün, comprehensive model for CO_2^- radicals in fossil tooth enamel: Implications for ESR dating. *Quat. Geochronol.* **6**, 82–97 (2011). doi: 10.1016/j.quageo.2010.09.001
49. R. Joannes-Boyau, R. Grün, Thermal behavior of orientated and non-orientated CO2− radicals in tooth enamel. *Radiat. Meas.* **44**, 505–511 (2009). doi: 10.1016/j.radmeas.2009.02.010
50. Q. Shao, J.-J. Bahain, C. Falgueres, J.-M. Dolo, T. Garcia, A new U-uptake model for combined ESR/U-series dating of tooth enamel. *Quat. Geochronol.* **10**, 406–411 (2014). doi: 10.1016/j.quageo.2012.02.009
51. A. P. Roberts *et al.*, Resolving the Origin of Pseudo-Single Domain Magnetic Behavior. *J. Geophys. Res. Solid Earth* **122**, 9534–9558 (2017). doi: 10.1002/2017JB014860

52. A. P. Roberts, C. R. Pike, K. L. Verosub, First-order reversal curve diagrams: A new tool for characterizing the magnetic properties of natural samples. *J. Geophys. Res. Solid Earth* **105**, 28461–28475 (2000). doi: 10.1029/2000JB900326
53. C. R. Pike, A. P. Roberts, K. L. Verosub, First-order reversal curve diagrams and thermal relaxation effects in magnetic particles. *Geophys. J. Int.* **145**, 721–730 (2001). doi: 10.1046/j.0956-540x.2001.01419.x
54. B. S. Singer, B. R. Jicha, N. Mochizuki, R. S. Coe, Synchronizing volcanic, sedimentary, and ice core records of Earth's last magnetic polarity reversal. *Sci. Adv.* **5**, w4621 (2019). doi: 10.1126/sciadv.aaw4621; pmid: 31457087
55. C. C. Gilbert, C. M. Steininger, J. M. Kibii, L. R. Berger, *Papio* Cranium from the Hominin-Bearing Site of Malapa: Implications for the Evolution of Modern Baboon Cranial Morphology and South African Plio-Pleistocene Biochronology. *PLOS ONE* **10**, e0133361 (2015). doi: 10.1371/journal.pone.0133361; pmid: 26287673
56. C. C. Gilbert, S. R. Frost, K. D. Pugh, M. Anderson, E. Delson, Evolution of the modern baboon (*Papio hamadryas*): A reassessment of the African Plio-Pleistocene record. *J. Hum. Evol.* **122**, 38–69 (2018). doi: 10.1016/j.jhevol.2018.04.012; pmid: 29954592
57. T. R. Edwards *et al*., Combining legacy data with new drone and DGPS mapping to identify the provenance of Plio-Pleistocene fossils from Bolt's Farm, Cradle of Humankind (South Africa). *PeerJ* **7**, e6202 (2019). doi: 10.7717/peerj.6202; pmid: 30656072
58. M. Kretzoi, Die Raubtiere von Gombaszög nebst einer übersicht der Gesamtfauna (Einbeitrag zur stratigraphie des Altquartaers). *Annales Musei nationalis hungarici* **31**, 88–157 (1938).
59. L. Werdelin, R. Dehghani, Carnivora, in *Palaeontology and Geology of Laetoli: Human Evolution in Context*, T. Harrison, Ed. (Springer, 2011), pp. 189–232.
60. L. Werdelin S. Peigné, Carnivora, in *Cenozoic Mammals of Africa*, L. Werdelin, W. J. Sanders, Eds. (Univ. California Press, 2010), pp. 603–658.
61. D. Roberts *et al*., Regional and global context of the Late Cenozoic Langebaanweg (LBW) palaeontological site: West Coast of South Africa. *Earth Sci. Rev.* **106**, 191–214 (2011). doi: 10.1016/j.earscirev.2011.02.002
62. L. Werdelin, M. Lewis, A revision of the genus *Dinofelis* (Mammalia, Felidae). *Zool. J. Linn. Soc.* **132**, 147–258 (2001). doi: 10.1111/j.1096-3642.2001.tb02465.x
63. H. Hemmer, Zur Nomenklatur und Verbreitung des Genus Dinofelis Zdansky, 1924. *Palaeont. Afr.* **9**, 785–789 (1965).
64. H. B. S. Cooke, *Dinofelis barlowi* (Mammalia, Carnivora, Felidae) cranial materialfrom Bolt's Farm, collected by the University of California African expedition. *Palaeontologica Africana.* **28**, 9–21 (1991).
65. R. Lacruz, A. Turner, L. R. Berger, New *Dinofelis* (Carnivora: Machairodontinae) remains from Sterkfontein Valley sites and a taxonomic revision of the genus in southern Africa. *Ann. Transvaal Mus.* **43**, 89–106 (2006).
66. A. Gentry, Bovidae, in *Cenozoic Mammals of Africa*, L. Werdelin, W. Sanders, Eds. (Univ. California Press, 2010), pp. 741–796.
67. K. E. Reed, thesis, State University of New York at Stony Brook (1996).
68. V. Watson, Composition of the Swartkrans bone accumulations, in terms of skeletal parts and animals represented, in *Swartkrans: a cave's chronicle of early man*, C. Brain Ed. (Transvaal Museum, 1993), pp. 35–74.
69. D. J. de Ruiter, Revised faunal lists for Members 1-3 of Swartkrans, South Africa. *Ann. Transvaal Mus.* **40**, 29–41 (2003).
70. D. J. de Ruiter *et al*., New *Australopithecus robustus* fossils and associated U-Pb dates from Cooper's Cave (Gauteng, South Africa). *J. Hum. Evol.* **56**, 497–513 (2009). doi: 10.1016/j.jhevol.2009.01.009; pmid: 19443017
71. D. Curnoe, R. Grün, J. F. Thackeray, Electron spin resonance dating of tooth enamel from Kromdraai B, South Africa. *S. Afr. J. Sci.* **98**, 540 (2002).
72. R. Pickering *et al*., Contemporary flowstone development links early hominin bearing cave deposits in South Africa. *Quat. Sci. Rev.* **306**, 23–32 (2011).
73. D. Lordkipanidze *et al*., A complete skull from Dmanisi, Georgia, and the evolutionary biology of early Homo. *Science* **342**, 326–331 (2013). doi: 10.1126/science.1238484; pmid: 24136960
74. C. J. Lepre, D. V. Kent, Chronostratigraphy of KNM-ER 3733 and other Area 104 hominins from Koobi Fora. *J. Hum. Evol.* **86**, 99–111 (2015). doi: 10.1016/j.jhevol.2015.06.010; pmid: 26190282
75. B. A. Wood, *Hominid Cranial Remains*, Koobi Fora Research Project, vol. 4 (Clarendon Press, 1991).
76. I. McDougall *et al*., New single crystal $^{40}Ar/^{39}Ar$ ages improve time scale for deposition of the Omo Group, Omo-Turkana Basin, East Africa. *J. Geol. Soc. London* **169**, 213–226 (2012). doi: 10.1144/0016-76492010-188
77. I. McDougall, F. H. Brown, Precise 40Ar/39Ar geochronology for the upper Koobi Fora Formation, Turkana Basin, northern Kenya. *J. Geol. Soc. London* **163**, 205–220 (2006). doi: 10.1144/0016-764904-166
78. D. R. Braun *et al*., Early hominin diet included diverse terrestrial and aquatic animals 1.95 Ma in East Turkana, Kenya. *Proc. Natl. Acad. Sci. U.S.A.* **107**, 10002–10007 (2010). doi: 10.1073/pnas.1002181107; pmid: 20534571
79. W. H. Y. Kimbel, Y. Rak, *Australopithecus sediba* and the emergence of *Homo*: Questionable evidence from the cranium of the juvenile holotype MH 1. *J. Hum. Evol.* **107**, 94–106 (2017). doi: 10.1016/j.jhevol.2017.03.011; pmid: 28526292
80. R. Joannes-Boyau *et al*., Elemental signatures of *Australopithecus africanus* teeth reveal seasonal dietary stress. *Nature* **572**, 112–115 (2019). doi: 10.1038/s41586-019-1370-5; pmid: 31308534
81. J. A. Ledogar *et al*., Mechanical evidence that *Australopithecus sediba* was limited in its ability to eat hard foods. *Nat. Commun.* **7**, 10596 (2016). doi: 10.1038/ncomms10596; pmid: 26853550
82. P. B. deMenocal, Climate and human evolution. *Science* **331**, 540–542 (2011). doi: 10.1126/science.1190683; pmid: 21292958
83. R. Potts, Environmental hypotheses of hominin evolution. *Am. J. Phys. Anthropol.* **107** (suppl. 27), 93–136 (1998). doi: 10.1002/(SICI)1096-8644(1998)107:27+<93::AID-AJPA5>3.0.CO;2-X; pmid: 9881524
84. M. A. Maslin, M. H. Trauth, Plio-Pleistocene East African Pulsed Climate Variability and its influence on Early Human Evolution, in *The First Humans: Origin and Early Evolution of the Genus* Homo, F. E. Grine *et al.*, Eds. (Springer, 2009), pp. 151–158.
85. Z. Zhu *et al*., Hominin occupation of the Chinese Loess Plateau since about 2.1 million years ago. *Nature* **559**, 608–612 (2018). doi: 10.1038/s41586-018-0299-4; pmid: 29995848
86. J. W. Adams, A. Olah, M. R. McCurry, S. Potze, Surface model and tomographic archive of fossil primates and other mammal holotype and paratype specimens of the Ditsong National Museum of Natural History, Pretoria, South Africa. *PLOS ONE* **10**, e0139800 (2015). doi: 10.1371/journal.pone.0139800; pmid: 26441324
87. S. Neubauer, P. Gunz, J.-J. Hublin, The pattern of endocranial ontogenetic shape changes in humans. *J. Anat.* **215**, 240–255 (2009). doi: 10.1111/j.1469-7580.2009.01106.x; pmid: 19531085
88. S. Neubauer, P. Gunz, Endocasts and the evo-devo approach to study human brain evolution in *Digital Endocasts: From Skulls to Brains*, E. Bruner, N. Ogihara, H. Tanabe, Eds. (Springer, 2018), pp. 173-190.
89. F. Spoor *et al*., Reconstructed *Homo habilis* type OH 7 suggests deep-rooted species diversity in early *Homo*. *Nature* **519**, 83–86 (2015). doi: 10.1038/nature14224; pmid: 25739632
90. S. Neubauer, P. Gunz, G. W. Weber, J.-J. Hublin, Endocranial volume of *Australopithecus africanus*: New CT-based estimates and the effects of missing data and small sample size. *J. Hum. Evol.* **62**, 498–510 (2012). doi: 10.1016/j.jhevol.2012.01.005; pmid: 22365336
91. W. H. Kimbel, B. Villmoare, From *Australopithecus* to *Homo:* The transition that wasn't. *Philos. Trans. R. Soc. B Biol. Sci.* **371**, 20150248 (2016). doi: 10.1098/rstb.2015.0248; pmid: 27298460
92. Z. Alemseged *et al*., A juvenile early hominin skeleton from Dikika, Ethiopia. *Nature* **443**, 296–301 (2006). doi: 10.1038/nature05047; pmid: 16988704
93. F. Marchand, *Ueber das Hirngewicht des Menschen* (B.G. Teubner, 1902).
94. J. DeSilva, J. Lesnik, Chimpanzee neonatal brain size: Implications for brain growth in *Homo erectus*. *J. Hum. Evol.* **51**, 207–212 (2006). doi: 10.1016/j.jhevol.2006.05.006; pmid: 16824583
95. K. Isler *et al*., Endocranial volumes of primate species: Scaling analyses using a comprehensive and reliable data set. *J. Hum. Evol.* **55**, 967–978 (2008). doi: 10.1016/j.jhevol.2008.08.004; pmid: 18817943
96. S. Neubauer, P. Gunz, U. Schwarz, J.-J. Hublin, C. Boesch, Brief communication: Endocranial volumes in an ontogenetic sample of chimpanzees from the Taï Forest National Park, Ivory Coast. *Am. J. Phys. Anthropol.* **147**, 319–325 (2012). doi: 10.1002/ajpa.21641; pmid: 22101940
97. S. Zuckerman, Age-changes in the chimpanzee, with special reference to growth of brain, eruption of teeth, and estimation of age; with a note on the Taungs ape. *Proc. Zool. Soc. Lond.* **98**, 1–42 (1928). doi: 10.1111/j.1469-7998.1928.tb07138.x
98. J. A. Catt, Palaeopedology manual. *Quat. Int.* **6**, 1–95 (1990). doi: 10.1016/1040-6182(90)90002-L
99. North American Commission on Stratigraphic Nomenclature (NACSN), 1981, Draft North American Stratigraphic Code: Canadian Society of Petroleum Geologists, Calgary, North American Stratigraphic Code. *American Assoc. Petrol. Geol. Bull.* **67**, 841–875 (1983).
100. P. N. Bullock, N. Fedoroff, A. Jongerius, *Handbook for Soil Thin Section Description* (Waine Research, 1985).
101. R. J. Joannes-Boyau, M. Duval, T. Bodin, MCDoseE 2.0 A new Markov Chain Monte Carlo program for ESR dose response curve fitting and dose evaluation. *Quat. Geochronol.* **44**, 13–22 (2018). doi: 10.1016/j.quageo.2017.11.003
102. M. Duval, R. Grün, Are published ESR dose assessments on fossil tooth enamel reliable? *Quat. Geochronol.* **31**, 19–27 (2016). doi: 10.1016/j.quageo.2015.09.007
103. B. M. Moskowitz, Methods for estimating curie temperatures of titanomagnetites from experimental Js-T data. *Earth Planet. Sci. Lett.* **53**, 84–88 (1981). doi: 10.1016/0012-821X(81)90028-5
104. R. Leonhardt, Analyzing rock magnetic measurements: The RockMagAnalyzer 1.0 software. *Comput. Geosci.* **32**, 1420–1431 (2006). doi: 10.1016/j.cageo.2006.01.006
105. R. J. Harrison, J. M. Feinberg, FORCinel: An improved algorithm for calculating first-order reversal curve distributions using locally weighted regression smoothing. *Geochem. Geophys. Geosyst.* **9**, Q05016 (2008). doi: 10.1029/2008GC001987
106. R. Egli, VARIFORC: An optimized protocol for calculating non-regular first-order reversal curve (FORC) diagrams. *Global Planet. Change* **110**, 302–320 (2013). doi: 10.1016/j.gloplacha.2013.08.003
107. D. P. Maxbauer, J. M. Feinberg, D. L. Fox, MAX UnMix: A web application for unmixing magnetic coercivity distributions. *Comput. Geosci.* **95**, 140–145 (2016). doi: 10.1016/j.cageo.2016.07.009
108. J. L. Kirschvink, The least-square line and plane and the analysis of palaeomagnetic data. *Geophys. J. R. Astron. Soc.* **62**, 699–718 (1980). doi: 10.1111/j.1365-246X.1980.tb02601.x
109. R. Fisher, Dispersion on a sphere. *Proc. R. Soc. London Ser. A* **217**, 512–515 (1953).
110. N. Guérin, Mercier, G. Adamiec, Dose rate conversion factors: Update. *Anc. TL* **29**, 5–8 (2011).
111. R. Grün, Beta dose attenuation in thin layers. *Anc. TL* **4**, 1–8 (1986).

ACKNOWLEDGMENTS

We thank the student excavators from the La Trobe University (LTU) Drimolen Palaeoanthropology and Geoarchaeology Field School and University of Victoria Field School, as well as the University of Florence Archaeological Mission to Drimolen. In particular, we thank LTU Ph.D. student R. Curtis who first found parts of the DNH 134 cranium. We thank D. Smith, J. Smith, and K. Nkosi, the landowners at Drimolen at various stages and who granted our permission to work at the site, in conjunction with the South African Heritage Resources Agency (SAHRA). The DNH 152 cranium is named after the landowner (Khethi) as he excavated with us on the field school and discovered the first tooth. We say a special thanks to our co-author Simon Mokobane for his many years of work at the site. Simon recently passed away from cancer and he will be remembered fondly by many generations of people who have worked at Drimolen. In recognition of this, we have named the DNH 134 cranium after him (Simon). This work would not have been possible without him. We thank D. Bilardello, M. Jackson, and J. Feinberg for their help and advice while measuring at the Institute of Rock Magnetism. We thank B. Zipfel for facilitating access to the hominin collections at the University of the Witwatersrand. **Funding:** The bulk of this research was funded by Australian Research Council Future Fellowship Grant FT120100399 to A.I.R.H. and ARC Discovery Grant DP170100056 to A.I.R.H., J.W.A., D.S.S., and R.J.-B. The U-Pb analysis was funded

by ARC DECRA DE120102504 to R.P. The US-ESR dating was supported by ARC DP140100919 to R.J.-B. Work at the site by the Italian Archaeological Mission was supported by a series of grants by the Italian Ministry of Foreign Affairs to J.M.-C.; C.M. thanks the National Research Foundation (African Origins Platform) for grants that supported the excavation and research at Drimolen. This work was also supported by a La Trobe University Postgraduate Research Scholarship and La Trobe University Internal Research grant to A.B.L., A.M., B.J.A., T.R.E., T.M., and R.C.S., and a Society of Antiquaries London research grant to J.M.M. Components of the palaeomagnetic work were conducted during a Visiting Research Fellowship to T.M. at the Institute for Rock Magnetism, University of Minnesota, supported through the National Science Foundation, USA. **Author contributions:** A.I.R.H. led the geology and dating program and undertook the palaeomagnetic analysis with T.M.; J.M.M., A.B.L., D.S.S., S.N., G.T.S., and C.M. undertook the analysis of the hominin remains. J.W.A., J.M., D.S.R., C.M., and S.B. undertook faunal analysis and biochronology. G.B. and A.I.R.H. undertook stratigraphic analysis and interpretation. G.B., A.M., T.R.E., and T.D. undertook micromorphological analysis. R.J.-B. undertook the US-ESR dating. B.J.A. undertook spatial and geographic information system analysis. J.H., J.W., and R.P. undertook uranium-lead dating and associated contextual analysis. M.V.C. and R.C.S. undertook studies of the archaeological material. A.B.L., S.B., J.M.M., and A.I.R.H. excavated the hominin crania. B.J.A. and C.W. undertook video and imaging of the site. A.I.R.H., S.B., C.M., and J.M.-C. directed excavations at different times that recovered the hominin material. C.M. initiated the dating program at Drimolen. All authors contributed to the writing of the paper. Research supporting this publication was undertaken by J.M., A.B.L., A.M., while completing a Ph.D. at La Trobe University. **Competing interests:** The authors declare no competing interests. **Data and materials availability:** All data are available in the main text or the supplementary materials. The fossils are curated at the University of the Witwatersrand hominin vault. Access for research is granted through the hominin access committee (bernhard.zipfel@wits.ac.za), including requests for the 3D scan data.

SUPPLEMENTARY MATERIAL

science.sciencemag.org/content/368/6486/eaaw7293/suppl/DC1
Tables S1 to S3
Movie S1

23 January 2019; accepted 11 February 2020
10.1126/science.aaw7293